Developmental Cell
Article

Organization of Embryonic Morphogenesis via Mechanical Information

Dipjyoti Das,[1,6] Dörthe Jülich,[1,6] Jamie Schwendinger-Schreck,[1,6] Emilie Guillon,[1] Andrew K. Lawton,[1] Nicolas Dray,[1] Thierry Emonet,[1,2] Corey S. O'Hern,[2,3,4] Mark D. Shattuck,[5] and Scott A. Holley[1,7,*]
[1]Department of Molecular, Cellular, and Developmental Biology, Yale University, New Haven, CT 06520, USA
[2]Department of Physics, Yale University, New Haven, CT 06520, USA
[3]Department of Mechanical Engineering and Materials Science, Yale University, New Haven, CT 06520, USA
[4]Department of Applied Physics, Yale University, New Haven, CT 06520, USA
[5]Department of Physics and Benjamin Levich Institute, City College of the City University of New York, New York, NY 10031, USA
[6]These authors contributed equally
[7]Lead Contact
*Correspondence: scott.holley@yale.edu
https://doi.org/10.1016/j.devcel.2019.05.014

SUMMARY

Embryonic organizers establish gradients of diffusible signaling molecules to pattern the surrounding cells. Here, we elucidate an additional mechanism of embryonic organizers that is a secondary consequence of morphogen signaling. Using pharmacological and localized transgenic perturbations, 4D imaging of the zebrafish embryo, systematic analysis of cell motion, and computational modeling, we find that the vertebrate tail organizer orchestrates morphogenesis over distances beyond the range of morphogen signaling. The organizer regulates the rate and coherence of cell motion in the elongating embryo using mechanical information that is transmitted via relay between neighboring cells. This mechanism is similar to a pressure front in granular media and other jammed systems, but in the embryo the mechanical information emerges from self-propelled cell movement and not force transfer between cells. The propagation likely relies upon local biochemical signaling that affects cell contractility, cell adhesion, and/or cell polarity but is independent of transcription and translation.

INTRODUCTION

Spemann and Mangold's discovery of embryonic organizers and subsequent theories of morphogens and positional information, and the experimental identification of morphogen gradients are seminal breakthroughs in developmental biology. We now understand that organizers establish gradients of diffusible signaling molecules that pattern the surrounding cells in a concentration-dependent manner (Lander, 2007; Müller et al., 2013). How morphogens interlink with mechanical forces is poorly understood, but recent studies have begun to integrate morphogen patterning with morphogenesis. For example, cell rearrangement sharpens the boundaries between expression domains downstream of noisy morphogen signaling in the vertebrate neural tube (Xiong et al., 2013). In the zebrafish shield, the equivalent of the Spemann-Mangold organizer, a positive feedback loop emerges in which a morphogen increases cell adhesion that then increases reception of the morphogen signal (Barone et al., 2017). During organogenesis, folding of the vertebrate gut epithelium creates local maxima of secreted signaling molecules that then pattern the crypt-villus axis required for gut homeostasis (Shyer et al., 2015).

Much like our understanding of morphogen signaling, insights into the role of mechanical forces in development have been pioneered by studies of both *Drosophila* and vertebrate gastrulation (Williams and Solnica-Krezel, 2017). To generalize, these forces are generated through actomyosin contractility and transmitted to adjacent cells via cell-cell and cell-ECM (extra-cellular matrix) adhesions that are linked to the cytoskeleton. We are just beginning to understand how coordination of these forces among cells can drive tissue morphogenesis (Heisenberg and Bellaïche, 2013; LeGoff and Lecuit, 2015). For example, the distribution of cell-ECM adhesions within a tissue is inversely correlated with the degree of cell displacement during *Drosophila* dorsal closure (Goodwin et al., 2016). A nice illustration of long-range organization via cellular forces is how internalization of the *Drosophila* endoderm generates supercellular tension that cell non-autonomously drives germband extension (Lye et al., 2015).

The vertebrate tail organizer (TO) functions within a flux of tail bud mesodermal progenitors to direct the elongation of the developing spinal column (Figure 1A) (Agathon et al., 2003; Beck and Slack, 1999; Beck et al., 2001). We previously tracked individual cell motion in the zebrafish tail bud, segmented the tail bud into four domains (excluding the notochord), and quantified collective cell behavior in these different domains (Lawton et al., 2013). The cells in the anterior dorsal medial domain of the tail bud are mostly spinal-cord precursors. Here, for simplicity, we refer to this domain as the posterior neural tube (PNT). These cells migrate posteriorly toward the dorsal-medial zone (DM). The DM contains rapidly moving neural-mesodermal progenitors (Martin and Kimelman, 2012; Wilson et al., 2009). DM cells differentiating into mesoderm migrate ventrally into the tail organizer and then bilaterally disperse to populate the left and right presomitic mesoderm (PSM) (Das et al., 2017; Lawton et al., 2013). The

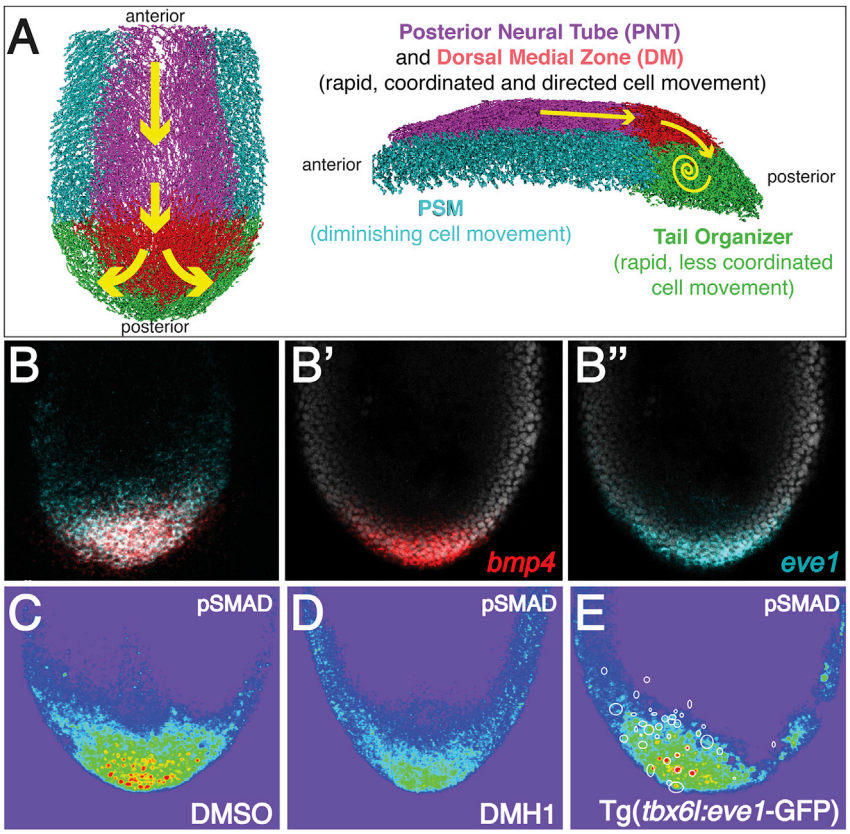

Figure 1. Bmp-*eve1* Signaling in the Zebrafish Tail Organizer

(A) A schematic of cell motion in the extending tail bud. Cell tracks are colored as indicated. The tail organizer is synonymous with the previously defined progenitor zone (Lawton et al., 2013).

(B–E) Overlapping mRNA localization for *bmp4* and *eve1* in the tail organizer (B). pSMAD localization in control (C), DMH1-treated (D), and transgenic embryos (E). Warmer colors indicate higher levels of Bmp signaling. Circles in (E) mark the location of transgene-expressing cells.

tail organizer is more fluid than the surrounding domains, and as these cells assimilate into the PSM, the tissue undergoes a fluid-to-solid transition in tissue mechanics (Lawton et al., 2013; McMillen and Holley, 2015; Mongera et al., 2018).

The tail organizer is located in the posterior tail bud, and both the mesoderm and epidermis express the secreted signaling proteins *bmp4* and *bmp2b* and the transcription factor *eve1* (Figures 1A–1B″) (Thisse and Thisse, 2005). Bmp signaling in the tail organizer is required for zebrafish body elongation (Connors et al., 2006; Pyati et al., 2005; Stickney et al., 2007; Yang and Thorpe, 2011). The Bmp inhibitors *chordin* and *noggin* are expressed in the posterior notochord and PSM, thus Bmp signaling is restricted to the posterior tail bud as indicated by phosphorylated SMAD (pSMAD) 1/5/8 immunolocalization (Figure 1C) (O'Neill and Thorpe, 2013; Row and Kimelman, 2009). *Even-skipped* (*eve* or *evx*) genes are adjacent to the *hox13* end of *hox* clusters suggesting a role in posterior animal development (Cruz et al., 2010; Li and Manley, 1998; McKay et al., 1999; Seebald and Szeto, 2011). Indeed, *eve1* overexpression produces duplicated tails, and *eve1* is expressed in ectopic TOs (Agathon et al., 2003; Barro et al., 1995; Connors et al., 2006; Cruz et al., 2010; Joly et al., 1993; Mullins et al., 1996; Row and Kimelman, 2009; Seebald and Szeto, 2011; Stickney et al., 2007; Yang and Thorpe, 2011). The patterns of *bmp* and *eve1/evx1* expression are conserved in *Xenopus* and mouse tail buds, and *bmp* and *evx1* have tail-inducing activity in *Xenopus* (Beck and Slack, 1999; Beck et al., 2001; Dush and Martin, 1992; Fainsod et al., 1994; Gofflot et al., 1997; Goldman et al., 2000; Ohta et al., 2007). In the mouse and chick, regulation of Bmp signaling from the ventral ectodermal ridge and mesoderm of the tail bud promotes the cessation of gastrulation and is required for subsequent tail bud elongation (Goldman et al., 2000; Ohta et al., 2007).

The consistent spatial expression pattern of zebrafish *eve1*, *bmp4*, and *bmp2b* in the tail organizer is maintained despite extensive cell movement (Figures 1A–1B″) (Dray et al., 2013; Fior et al., 2012; Lawton et al., 2013; Mara et al., 2007; Steventon et al., 2016). Here, we investigate how the tail organizer sustains itself and orchestrates body elongation. We find that the tail organizer regulates cell flux into the organizer downstream of Bmp signaling and non-cell-autonomously via mechanical information. The *in vivo* data and computational modeling suggest that the mechanical information initiates a cell-to-cell relay that alters the movement of neighboring cells and propagates through the migrating flux of cells over distances beyond the range of Bmp signaling.

RESULTS

Perturbation of Tail Organizer Signaling

We abrogated tail organizer function during trunk elongation using DMH1, a chemical inhibitor of Bmp receptor kinase signaling that enables temporal control of inhibition (Hao et al., 2010). The strongest reduction in pSMAD levels was observed 2 h post-treatment (Figures 1D and 2A). *bmp4* and *eve1* transcription are sensitive to reduction of Bmp signaling while *bmp2b* transcription is not dependent upon Bmp signaling (Figures 2B and S1A).

We performed a targeted spatial perturbation of organizer signaling by mosaically coexpressing *eve1* and GFP under the control of the *tbx6l* enhancer (Figure 2C) (Dray et al., 2013; Szeto and Kimelman, 2004). *tbx6l* expression largely overlaps *eve1* expression, thus the transgene mosaically disrupts the levels and regulation of *eve1* within its normal expression domain in the posterior tail bud. Mosaic overexpression of *eve1* elevated total pSMAD levels and increased pSMAD in both transgenic and nontransgenic cells within the TOTO, producing a more heterogeneous pattern (n = 12) (Figures 1E and 2D). The *eve1* transgene also increased transcription of *bmp2b*, *bmp4*, and

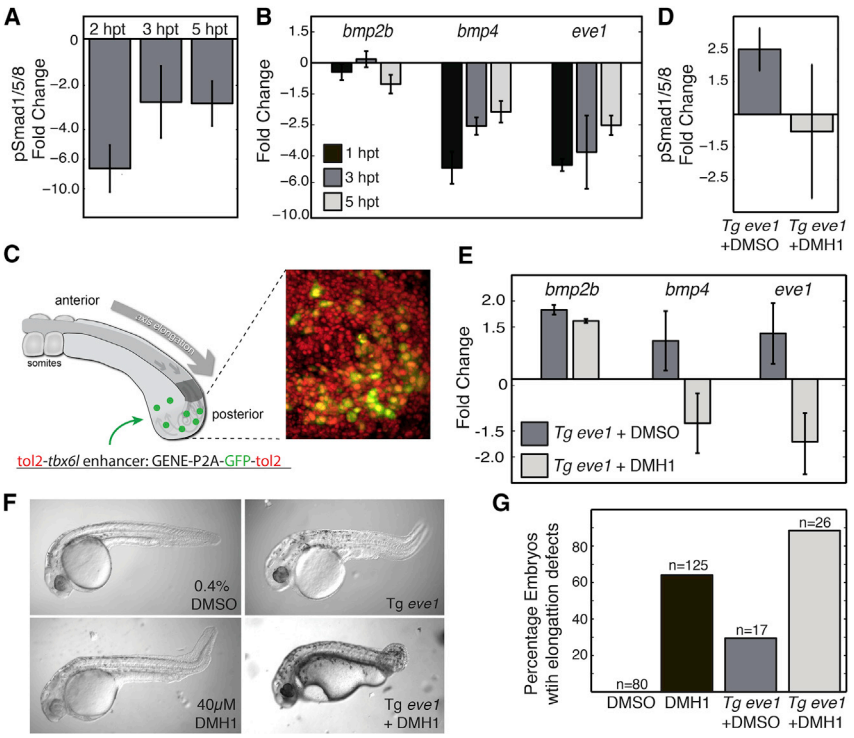

Figure 2. Temporally and Spatially Controlled Perturbation of the Tail Organizer

(A and B) Western blot for pSmad (A) and qRT-PCR for nascent transcription (B) of pooled, dissected tail buds from embryos treated with DMH1 or DMSO at the 5-somite stage. pSmad levels (A) and *bmp4* and *eve1* transcription are reduced 1–5 h post-DMH1 treatment (hpt) relative to DMSO-treated controls. n = 3 replicates for each time point.

(C–E) A local perturbation of the tail organizer is introduced in transient transgenics that express *eve1* along with GFP using the *tbx6l* enhancer. On the right, an experimental image of a tail organizer is shown in which nuclei of all cells are labeled with nls-RFP (red) and transgenic cells are labeled with GFP (green). Transgenic expression of *eve1* increases pSmad levels (D) as well as *bmp2b*, *bmp4*, and *eve1* transcription (E). Blocking the Bmp receptor with DMH1 eliminates the increase in pSmad (D) and *bmp4* and *eve1* transcription, but not *bmp2b* transcription (E). Measurements were made 3 h post-DMH1 treatment. n = 3 experimental replicates for each condition.

(F) Representative images of body elongation phenotypes following perturbation of the tail organizer.

(G) A summary of the percent of embryos with body elongation defects. Total number of embryos from at least three experimental replicates are indicated. Error bars denote the standard error. See also Figure S1.

endogenous *eve1* (Figure 2E). Transgenic embryos treated with DMH1 showed wild-type levels of pSMAD, but reduced transcription of both *eve1* and *bmp4* (Figures 2D and 2E). These data indicate that the TO is sustained within the flux of cells transiting the organizer via positive feedback between *eve1*, *bmp4*, and *bmp2b*.

DMH1 treatment, transgenic expression of *eve1*, and transgenic expression of *Tg eve1* + DMH1 treatment beget defects in body elongation with the latter producing the most frequent and strongest defects (Figures 2F and 2G). Given that *Tg eve1* + DMH1 have normal levels of Bmp signaling in the tail organizer, these data indicate that wild-type body elongation requires the regulated spatiotemporal pattern of Bmp signaling produced by the *bmp1-eve1* circuit. To determine the kinematic basis of the elongation phenotypes, we systematically analyzed cell motion in the tail bud after perturbation of the tail organizer. We acquired 3D confocal time-lapses of nuclear localized Red Fluorescent Protein (RFP) in four DMSO-treated control embryos, four DMH1-treated embryos, three transgenic DMSO-treated embryos, and three transgenic DMH1-treated embryos.

Cell motion in the tail organizer (TO) is aberrant in both DMH1 and *Tg eve1* + DMH1 embryos. Cell track straightness is reduced in both conditions, and the mean coefficient of variation (CV) of cell track speed is increased in DMH1 embryos (Figures 3A and 3B). We examined the mean square displacement (MSD), and modeled the data using a diffusion coefficient and directional velocity (Figures 3C and 3D) (Dray et al., 2013; Monnier et al., 2012). The directional velocity is reduced in the TO of DMH1 embryos (Figure 3D). Cell flux through the TO includes a medial domain comprised of both a dorsal-to-ventral flow and a medial-to-lateral flow that are segregated from flows on the lateral periphery that are predominantly posterior to anterior and ventral to dorsal (Figures 3G and S2). These flows intermix after perturbation of TO signaling, and the disruption of the dorsal-to-ventral flow likely obstructs cell flow into and through the TO, particularly in *Tg eve1* + DMH1 embryos.

Outside of the TO in the PNT and DM, cell track straightness is reduced and the mean CV of cell track speed was increased in all experimental conditions (Figures 3A and 3B). The diffusion coefficient normally spikes in the TO, but in both *Tg eve1* and *Tg eve1* + DMH1 embryos, the DM diffusion coefficient is increased, and this increase extends into the PNT in *Tg eve1* + DMH1 embryos (Figure 3C). Reduction in directional velocity was also observed in the DM of DMH1 embryos (Figure 3D). These data indicate that perturbation of TO signaling affects cell motion outside of the organizer. To measure the effect these perturbations have on collective cell behavior, we examined global order of cell motion. Global order within each domain is quantified via the polarization (Φ), which provides a normalized measure of the coherence of cell velocities. DM global order is reduced in each experimental condition while PNT global order is reduced in *Tg eve1* + DMH1 embryos (Figure 3F). Local order quantifies the alignment of instantaneous velocities within a 20-μm radius of each cell and provides the statistics of the alignment angles expressed in a cumulative distribution function (CDF). While the global and local order typically correlate, there are experimental perturbations that cause them to differ (Das et al., 2017). We were particularly interested in the apparent long-range effects of the perturbations observed in the PNT and quantified local order in this domain. We found that the local order of cell motion is reduced in the PNT of *Tg eve1* + DMH1 embryos (Figures 3E and S3A).

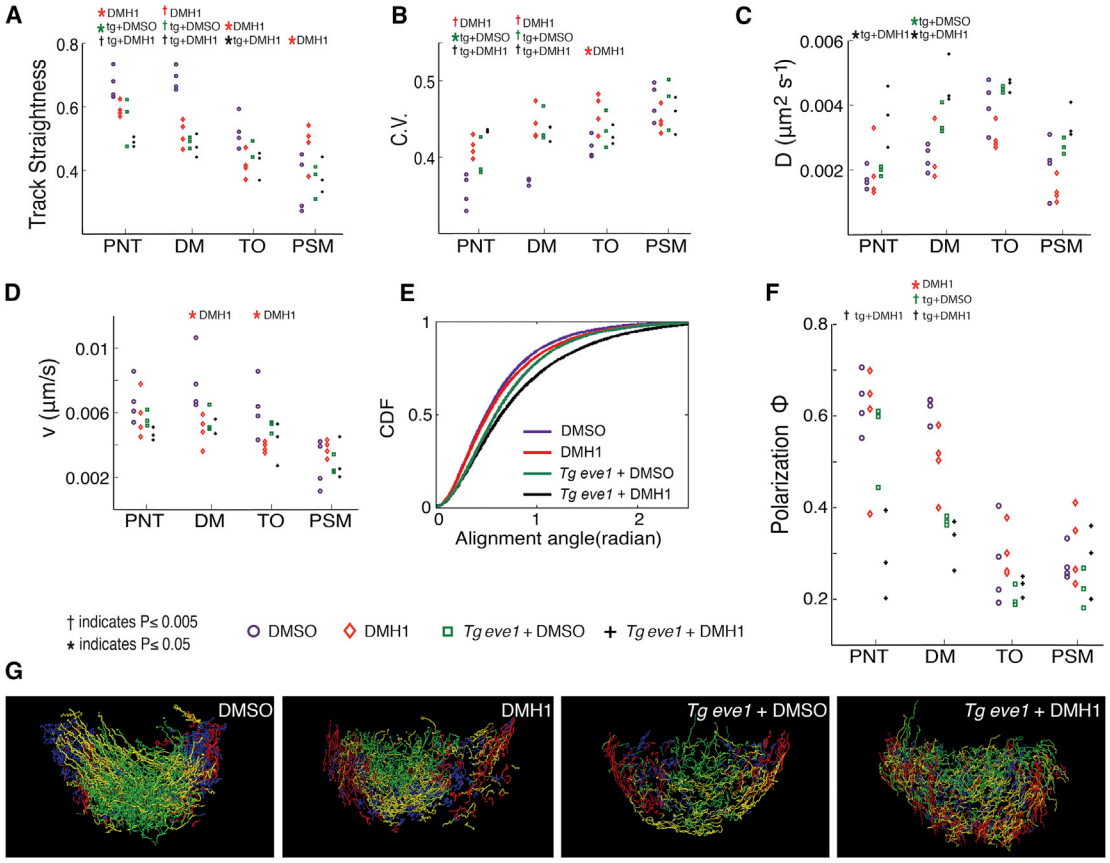

Figure 3. Perturbation of the Tail Organizer Has Long-Range Effects on Tail Bud Cell Motion

Treatments that gave a significant change from wild type in a given tail bud domain are indicated at the top of each panel.

(A) Cell track straightness.

(B) Mean coefficient of variation of cell track speed.

(C and D) Diffusion coefficient (C) and directional velocity (D) obtained by fitting the data to a MSD model.

(E) Local order as measured by the CDF (cumulative distribution function) of the local alignment angle. The CDFs for DMSO-treated controls and *Tg eve1* + DMH1 embryos differ ($p < 0.05$, t test). A steeper curve indicates more ordered cell motion.

(F) Global order as measured by polarization Φ.

In panels (A)–(D) and (F), the metrics are shown for four domains of the tail (PNT, DM, TO, and PSM). In (E), local order is shown only for the PNT. p Values determined by t test.

(G) Cell flow within the TO visualized by displaying only cell tracks with the greatest displacement from dorsal to ventral (green), medial to lateral (yellow), posterior to anterior (red), and ventral to dorsal (blue). In DMSO control embryos, the dorsal-to-ventral flow is concentrated medially while the posterior-to-anterior and ventral-to-dorsal flows are concentrated laterally. This represents the predominant pattern of cell flow through the tail organizer from the DM and into the PSM. In experimental embryos, these flows are less well segregated indicating a more disordered flux through the tail organizer, particularly in *Tg eve1* + DMH1 treated embryos. See also Figures S2 and S3.

Long-Range Effects of Organizer Perturbation

The observations that transgenic expression of *eve1* in the tail organizer and inhibition of Bmp signaling, which is restricted to the tail organizer, are sufficient to affect cell motion in the PNT suggest a long-range organizing function for the tail organizer beyond the range of Bmp signaling. We hypothesized that the long-range orchestration of cell motion by the tail organizer is mechanical and mediated by a relay between migrating cells. In the embryo, there is unlikely to be force transmitted from cell-to-cell due to viscous drag. Instead, physical contact between cells could induce a biochemical response such as cell-contact-mediated repulsion or changes in cell contractility, adhesion, or polarity that alter the active migration of the cell. This relay would pass posterior to anterior from cell-to-cell until it dissipates due to both viscous drag and resistance by the predominant anterior-to-posterior flow of cells in the neural tube.

This relay mechanism has similarities to a pressure front traveling through granular media and jammed matter such as glassy and gel-like materials (Boudet et al., 2009; Rericha et al., 2002). However, this phenomenon is not well studied in active matter or biological systems. To explore this mechanism theoretically, we developed a 3D computational model of the elongating tail bud that represents cells as self-propelled elastic spheres (Figures 4A and S4A) (Gönci et al., 2008; Szabó et al., 2006). As in our prior 2D models, there are adhesive and repulsive interactions between cells and a propensity for neighboring cells to align their instantaneous velocities (Das et al., 2017; Lawton et al., 2013) (see Supplemental Information for details). Note that repulsion

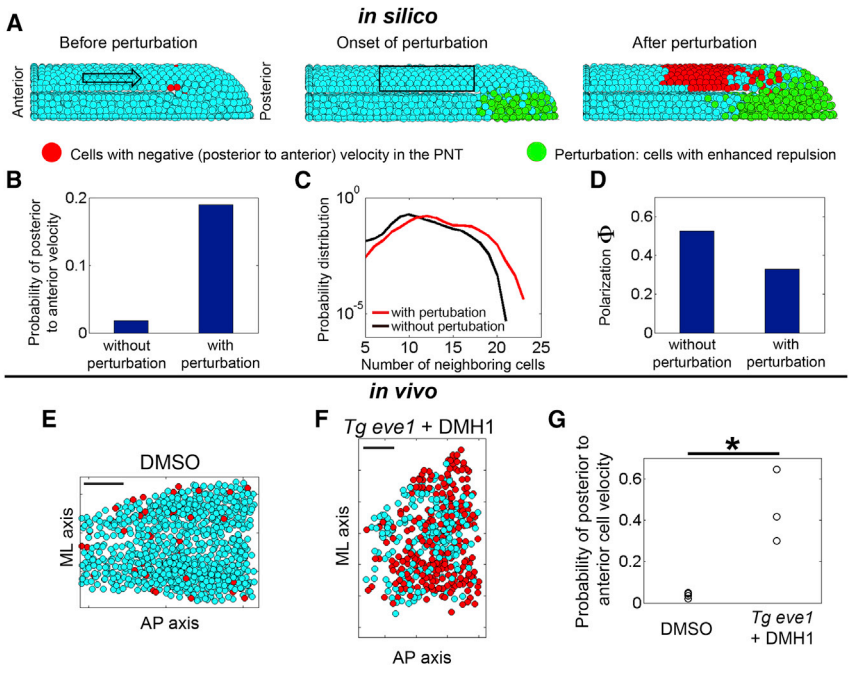

Figure 4. Analysis of Mechanical Information Propagation Following a Perturbation in the Tail Organizer Using 3D Computer Simulations and *In Vivo* Data

(A–D) Simulations: (A) before the perturbation (left panel), the overall flow of PNT cells is from anterior-to-posterior (arrow), though a few cells may stochastically move posterior to anterior at any instant (3 red cells). The perturbation is then introduced (middle panel) by stochastically increasing cell-cell repulsion in tail organizer cells (green). After the onset of the perturbation (right panel), a large group of cells in the PNT display posterior-to-anterior velocities (red cells), and the front of this disturbance propagates posterior to anterior over time (see Video S1). (B) The probability of posterior-to-anterior cell velocities in the PNT is higher after the perturbation ($p < 0.05$, t test). (C) Cell density is quantified via the probability distribution of the number of neighboring cells. These two probability distributions (before and after perturbation) show that the number of neighboring cells is higher in the PNT after perturbation ($p < 0.05$, t test). (D) Global order in cell motion, polarization Φ, is reduced in the PNT after the perturbation ($p < 0.05$, t test). All quantities in panels (B)–(D) are calculated by sampling within a fixed volume (black rectangle in [A]) over 30 simulations with and 30 simulations without perturbation. In (B) and (D), the standard deviations are <6%.

(E–G) Experiments: snapshots of cells of the PNT in (E) a DMSO-treated control embryo (see Video S2) and (F) a DMH1-treated *tbx6l:eve1*-transgenic (see Video S3). Red dots indicate cells with a posterior-to-anterior velocity. Scale bars in (E) and (F) represent 50 μm. (G) *Tg eve1* + DMH1 embryos ($n = 3$) have an increased probability of PNT cells having a posterior-to-anterior velocity relative to DMSO control embryos ($n = 4$) ($p < 0.05$, t test).

in the simulations may represent a number of *in vivo* mechanisms such as volume exclusion between cells, as two cells cannot occupy the same space, as well as biochemical processes such as contact-mediated repulsion.

Analysis of pressure fronts in granular matter suggests that a disturbance created by a local perturbation can travel through the material (Boudet et al., 2009; Rericha et al., 2002). Thus, to probe the transmission of mechanical information in our model, we introduced a local perturbation by increasing the repulsion between cells in the organizer. The perturbation is switched on stochastically in individual cells within the tail organizer to mimic transgene expression in experiments (Figure 4A). Consistent with the *in vivo* phenotype of *Tg eve1* + DMH1 embryos, the perturbation decreases cell track straightness and the mean CV of cell track speed in both the PNT and TO (Figures S4B and S4C).

If mechanical information is being transmitted from the TO to the PNT, the perturbation would mostly disturb the anterior-posterior component of cell velocities, and this disturbance should propagate posterior to anterior through the PNT. Therefore, in the presence and absence of the perturbation, we examined the probability of posterior-to-anterior instantaneous velocities, which are directed oppositely to the general anterior-to-posterior flow of cells in the PNT. We found that the perturbation increased the probability of posterior-to-anterior cell velocities in the PNT (Figures 4A, 4B, and S4D; Video S1). The perturbation also increased cell density within the PNT as reflected by a shift in the probability distribution of the number of cell neighbors (Figures 4C and S4E). This theoretical result is consistent with local jamming of cells, similar to a traffic jam on a highway. A traffic jam starts from the site of an accident and then travels against the flow of traffic as a disturbance. The presence of competing cells moving forward and backward in the PNT following the perturbation decreases global order (Figures 4D and S4F). This lower polarization (Φ) *in silico* is again consistent with the observed *in vivo* phenotype of *Tg eve1* + DMH1 embryos.

We reexamined the *in vivo* data for the signatures of mechanical information suggested by this theory. Indeed, *Tg eve1* + DMH1 embryos exhibit an increased probability of posterior-to-anterior cell velocities in the PNT (Figures 4E–4G and S3B). Thus, the computer simulations provide a theoretical mechanism for the propagation of mechanical information in the tail bud. The information is transmitted as disturbance, which travels posterior to anterior, and then damps out due to the combined influence of viscosity and the competing active cell migration from anterior-to-posterior (Figures S4G–S4I).

Wnt and Fgf Signaling in the Tail Organizer

Wnt and Fgf signaling are both prominent in the zebrafish tail organizer and abrogation of either signaling pathway causes body elongation defects (Das et al., 2017; Fürthauer et al., 2002; Lawton et al., 2013; Row and Kimelman, 2009; Sawada et al., 2001; Steventon et al., 2016). Thus, it is possible that Bmp signaling could induce long-range effects indirectly by modulating Fgf or Wnt signaling. We examined expression of Wnt and Fgf target genes after DMH1 treatment and in *Tg eve1* + DMSO and Tg *eve1* + DMH1 embryos. DMH1 treatment alters *axin2*, *dkk1*, *sef*, and *sprouty* transcription (Figure S1A). However, *Tg eve1* and *Tg eve1* + DMH1 embryos exhibit similar levels of Wnt and Fgf target gene expression meaning that

alteration of Wnt and Fgf signaling does not explain the stronger long-range effects observed in *Tg eve1* + DMH1 embryos (Figure S1B).

Previously, we pharmacologically inhibited Fgf receptor signaling using SU5402 and reduced Wnt signaling by overexpression of *notumn1a* (Lawton et al., 2013). The mean CV of cell track speed is increased and track straightness is reduced after either Fgf or Bmp inhibition, but the directional velocity is only reduced in DMH1 and *Tg eve1* + DMH1 embryos. *notum1a* overexpression did not change any of these metrics (Das et al., 2017; Lawton et al., 2013). Thus, DMH1 embryos and *Tg eve1* + DMH1 embryos exhibit stronger tail organizer cell motion defects than reduction of Wnt or Fgf signaling. Accordingly, we do not observe an increase in posterior-to-anterior cell velocities in the PNT of embryos with reduced Wnt or Fgf signaling (Figure S3C). All together, these data indicate that the long-range effects observed in *Tg eve1* + DMH1 embryos are unlikely to be mediated by changes in Wnt or Fgf signaling.

Estimating the Speed of Mechanical Information

To estimate the rate at which mechanical information propagates, we displayed the mean anterior-to-posterior cell velocity as a heatmap plotted as a function of position along the anterior-posterior axis and time (Figure 5). In computer simulations, a disturbance of mean velocity propagates anteriorly after an increase in cell repulsion in the tail organizer. This disturbance appears as the purple flare (Figure 5A). We divided the plot into three time intervals representing the states before perturbation, immediately after perturbation, and long after perturbation. These three plots reflect the outcomes of the *in vivo* experiments in which we have less precise control of the perturbation. The propagation rate of the front of the disturbance is given by the slope of the flare (Figure 5A, lower middle plot). This propagation damps out due to viscosity and resistance from the predominant anterior-to-posterior cell flow, and the velocity field slowly returns to a normal state (Figure 5A, lower right plot).

We sought to replicate the *in silico* experiment *in vivo* by delaying the addition of DMH1 to *Tg eve1* embryos. In prior experiments, DMH1 was added 2 h before the start of the time-lapse (and before the embryos were mounted for imaging) to ensure that Bmp inhibition had been established. Here, we added DMH1 to *Tg eve1* embryos after embryos had been mounted for imaging and just before the start of the time-lapse. The objective was to image the onset of the Bmp inhibition and visualize any posterior-to-anterior propagation of disturbance in the cell velocities. Analysis of wild-type embryos and *Tg GFP* embryos produced velocity heatmaps similar to those observed in simulations before and long after perturbation (Figures 5B, 5C, S5A, and S5C). Plots of global order of cell motion (polarization Φ) in the PNT of these control embryos were relatively stable over time (Figures S5B and S5D). *Tg eve1* + DMH1 embryos exhibited two classes of phenotypes: group 1 (5 of 9 embryos) and group 2 (4 of 9 embryos). Group 1 had velocity heatmaps and polarization Φ values resembling controls (Figures S5E and S5F). By contrast, group 2 exhibited heatmaps with propagating posterior-to-anterior disturbances in mean velocity and highly variable polarization Φ values (Figures 5D, S5E, and S5G). Group 2 *Tg eve1* + DMH1 embryos also displayed evidence of mechanical information in the form of an increase in the probability of posterior-to-anterior cell velocities compared to group 1 *Tg eve1* + DMH1 embryos and *Tg GFP* controls (Figure S5H). Thus, experimental variability produces two classes of embryos with group 1 indistinguishable from controls and group 2 exhibiting evidence of propagation of mechanical information after perturbation. This range of phenotypes likely arises from the stochasticity of transgene expression and variation in DMH1 absorption in embryos mounted in low-melt agarose for imaging. Using the heatmaps, we estimated the maximum and minimum rates of posterior-to-anterior propagation of the disturbance (Figures 5D and S5E). The average propagation speed is estimated at 1 μm per min.

Increasing Cell Contractility in the Tail Organizer Induces Retrograde Motion in the PNT

To more directly examine mechanical information transfer, we generated a targeted mechanical disruption of the TO and quantified cell motion in the PNT. We mosaically increased actomyosin contractility in the TO via expression of an inhibitor of myosin phosphatase (*cpi-17*) under the control of the *tbx6l* enhancer. *cpi-17* has been shown to modulate cell migration during zebrafish gastrulation (Weiser et al., 2009). Moreover, an increase in actomyosin contractility mimics the increase in cell repulsion in our simulations. *Tg cpi-17* embryos exhibit a higher incidence of early developmental and body elongation defects compared to *Tg GFP* controls (Figures 6A and 6B). Embryos with severe body malformations are not suitable for our analysis of cell motion. Therefore, we used embryos that exhibited relatively mild phenotypes, typically retarded body elongation.

We examined tail bud expression of Bmp, Wnt, and Fgf target genes in *Tg cpi-17* tail buds (Figure 6C). Bmp and Fgf target gene expression were not altered relative to *Tg GFP* controls. One Wnt target, *dkk1*, exhibited a small decrease while the other Wnt target, *axin2*, was unchanged. Since we do not observe evidence of mechanical information after stronger perturbation of Wnt signaling (Figure S3C), any alteration in PNT cell motion in *Tg tbx6l:cpi-17* embryos should not be a consequence of altered tail organizer signaling.

Mosaic expression of *cpi-17* in the tail organizer reduces global order (polarization Φ) as well as local order in the PNT revealing a long-range effect of a local mechanical perturbation of the organizer (Figures 6H, S3D, and S3E). As predicted by theory, the mechanical information correlates with an increase in the probability of posterior-to-anterior cell velocity in the PNT as well as an increase in cell density (Figures 6D–6G). These data reveal a long-range effect of mechanical perturbation of the vertebrate tail organizer.

DISCUSSION

Here, we find that the zebrafish tail organizer orchestrates morphogenesis over distances beyond the range of Bmp signaling. This long-range organization is a secondary effect downstream of canonical organizer cell signaling and likely propagates through local, adhesive, and repulsive interactions between neighboring cells (Figure 6I). In other words, there is no transfer of force from one cell to another since viscous drag leads to overdamping. Thus, in contrast to pressure front propagation in granular media and other jammed materials that is

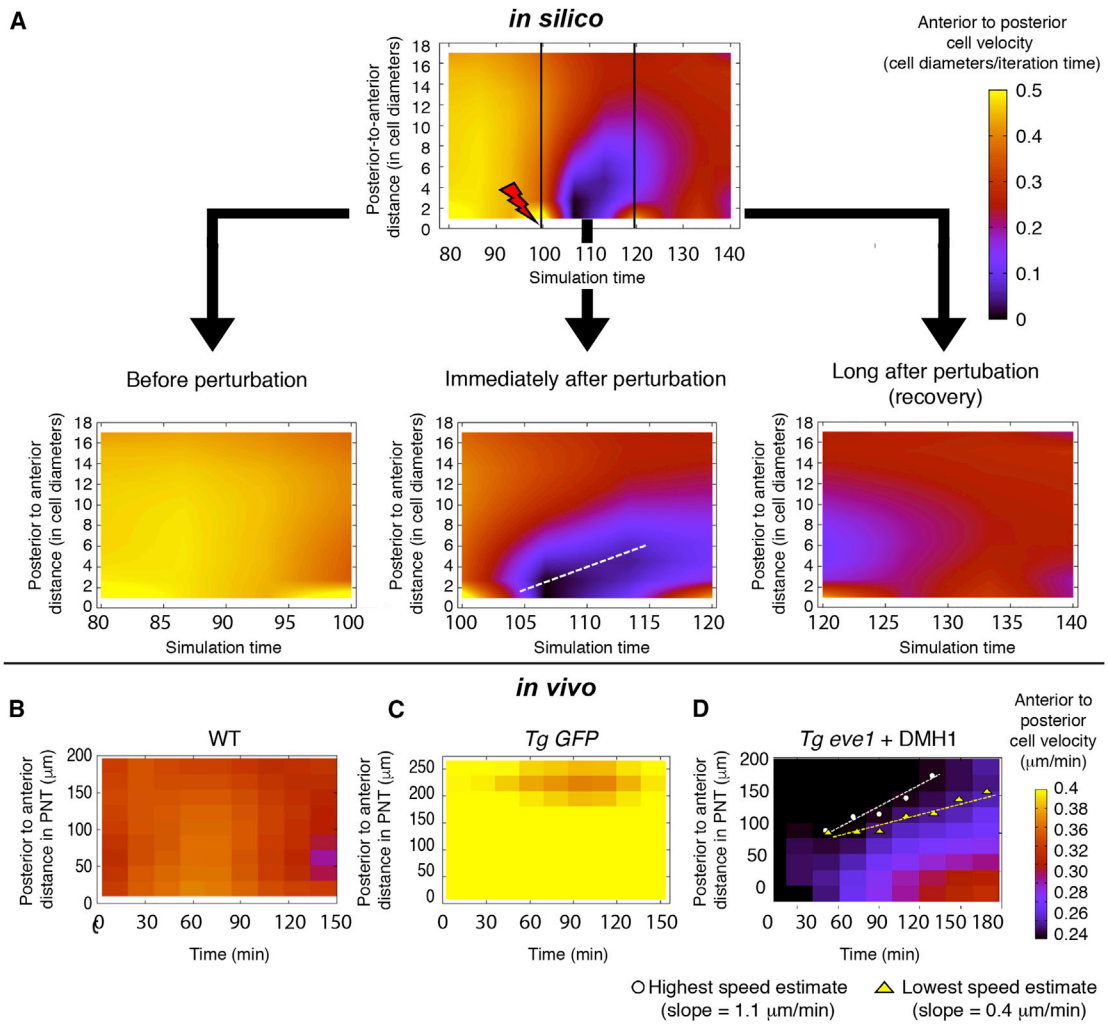

Figure 5. Estimating the Propagation Speed of Mechanical Information

(A) Computer simulations were performed with the perturbation triggered at time point 100 as described in Figure 4. Mean anterior-to-posterior cell velocity was plotted as heatmap as a function of posterior-to-anterior distance along the PNT and time. The mechanical information is revealed by the propagation of a disturbance in mean cell velocity from posterior to anterior (the purple flare). The plot was subdivided into three time intervals to increase the temporal resolution: before perturbation, immediately after perturbation, and long after perturbation. The speed of the posterior-to-anterior propagation of the mechanical information is estimated from the slope of the purple flare representing the disturbance over time (dashed line). In simulations, time is measured in units of 30 *in silico* iterations and the length is in units of cell diameters.

(B) The heatmaps for wild-type embryos are relatively uniform much like the simulations before or long after perturbation (see also Figure S5A).

(C) *Tg tbx6l:GFP* transgenic control embryos produce heatmaps that are relatively uniform (see also Figure S5C).

(D) *Tg tbx6l:eve1-GFP* embryos treated with DMH1 at the onset of imaging exhibit heterogenous heatmaps. Four of nine embryos exhibited the posterior-to-anterior propagation of a disturbance in mean anterior-to-posterior cell velocity. We estimated the maximum and minimum slope of the propagation for each of these embryos (see also Figures S5E–S5H).

induced by an external force, mechanical information emerges from a relay of cell intrinsic forces. The propagation is likely mediated by biochemical signaling that affects cell contractility, cell adhesion, and/or cell polarity, but is independent of transcription and translation.

The posterior tail bud is a complex cell-signaling domain with active Fgf, Wnt, and Bmp signaling, all of which have distinct effects on cell movement and cell fate. Fgf and Wnt are in gene regulatory networks that govern segmental patterning of the paraxial mesoderm and differentiation of bipotential neural-mesodermal progenitors (Gouti et al., 2017; Pourquié, 2011). Inhibition of Fgf decreases the speed of cell motion in the posterior tail bud of the chick, and in zebrafish, Fgf inhibition increases variability in cell speed and decreases track straightness in the posterior tail bud and reduces convergence in the PSM (Bénazéraf et al., 2010; Lawton et al., 2013; Steventon et al., 2016). Partial inhibition of Wnt signaling via injection of moderate levels of *notum1a* mRNA increases ordered cell motion in the DM, which in turn leads to loss of symmetric elongation (Das et al., 2017; Lawton et al., 2013). The increased order is likely due to inhibition of a two-step epithelial to mesenchymal transition (EMT) in neural-mesodermal progenitors (Manning and Kimelman,

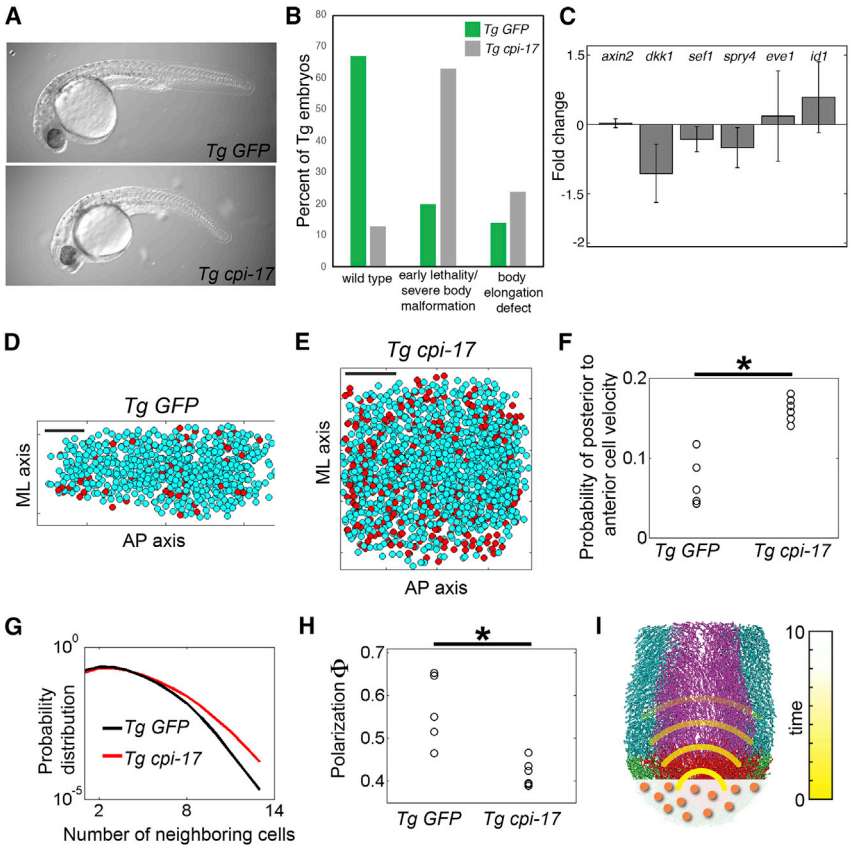

Figure 6. Mechanical Information Propagation after Increasing Cell Contractility in the Tail Organizer

(A) Transient *tbx6l* transgenics expressing either GFP (control) or *cpi-17* and GFP in the tail organizer.

(B) *Tg tbx6l:GFP* transgenics produce mostly normal embryos (3 experiments; n = 363) whereas *Tg tbx6l:cpi-17* embryos (4 experiments; n = 416) exhibit a high frequency of early developmental defects and embryos with abnormal body elongation.

(C) Nascent transcription of Wnt, Fgf, and Bmp target genes was examined by qRT-PCR on pooled dissected tail buds. Expression in *Tg tbx6l:cpi-17* tail buds was normalized to expression in *Tg tbx6l:GFP* controls. Data are averages from three independent experiments and display standard error.

(D and E) Snapshots of cells of the PNT in (D) a *Tg tbx6l:GFP* control (see Video S4) and (E) a *Tg tbx6l:cpi-17* embryo (see Video S5). Red dots indicate cells with a posterior-to-anterior velocity. Scale bars in (D) and (E) represent 50 μm.

(F) The probability of posterior-to-anterior cell velocities in the PNT in five *Tg tbx6l:GFP* controls and six *Tg tbx6l:cpi-17* embryos.

(G) Cell density in the PNT is displayed via the probability distribution of the number of neighboring cells. Each probability distribution is obtained by pooling the data from each experimental condition. These two probability distributions differ ($p < 0.05$, t test), and show that cell density is higher in *Tg tbx6l:cpi-17* embryos.

(H) Global order of PNT cell velocities as measured by the polarization Φ.

(I) Mechanical information (yellow) extends the sphere of influence of the tail organizer beyond that of a secreted signaling molecule (orange).

Asterisks denote $p < 0.05$ (t test).

2015). The first step in the EMT is regulated by Wnt and the second step is regulated by Fgf (Goto et al., 2017). This integration of Wnt and Fgf signaling is observed in the extensive cross talk between the two pathways in the zebrafish tail bud (Stulberg et al., 2012). Data presented here indicate that Bmp signaling exhibits some cross-regulation with Fgf and Wnt. Indeed, prior studies found that Bmp signaling opposes cell fate specification by Wnt and Fgf. Tail bud Bmp signaling promotes vasculature and tail-fin cell fates in zebrafish (Connors et al., 2006; Pyati et al., 2005; Row et al., 2018). Bmp signaling promotes vascular fates by increasing expression of *id* genes, which then inhibit the function of basic helix loop helix transcription factors that specify paraxial mesoderm cell fates downstream of Wnt and Fgf signaling (Row et al., 2018).

Within the tail organizer, Bmp signaling increases the directional velocity and promotes ordered cell flow, yet the flux of cells through the organizer is constrained by the requirement to maintain Bmp signaling. Cells must secrete sufficient Bmp protein while transiting the organizer to activate the *bmp-eve1* positive feedback in newly arrived cells. If this positive feedback is weakened, then the flux through the organizer must be reduced in order to maintain the organizer signaling domain. Cell flux through the tail organizer is characterized by a medial domain of both dorsal-to-ventral flow and medial-to-lateral flow that is segregated from flows moving posterior to anterior and ventral to dorsal along the lateral sides of the organizer. In *Tg eve1* + DMH1 embryos, these flows are intermixed, and the loss of the dorsal-to-ventral channel likely creates congestion that leads to the local decrease in cell velocities that propagates from posterior to anterior in the form of a disturbance. This decrease in cell speed may help maintain tail organizer signaling domain albeit at the cost of retarding tail elongation.

In contrast to the positive feedback between *bmp4* and *eve* in the tail organizer, *eve1* represses *bmp2b*, *bmp4*, and *eve1* transcription on the ventral side of the zebrafish gastrula (Figure S1C) (Cruz et al., 2010). This inversion in gene regulation is also observed in the Fgf regulation of *brachyury/ntla* in which Fgf promotes *brachyury/ntla* expression during gastrulation but inhibits *brachyury/ntla* expression in the tail bud during body elongation (Goto et al., 2017). These switches in regulatory feedback may underlie the transition from gastrulation to tail bud elongation.

We estimate that the mechanical information in the PNT travels at roughly 1 μm per min when measured at 18°C, which is a similar order of magnitude to the 0.39-μm per min average anterior-to-posterior velocity of PNT cells in wild-type embryos when measured at 18°C (Das et al., 2017). Zebrafish are ectothermic, and their rate of development increases dramatically with the temperature at which they are raised. Thus, one would expect the propagation of mechanical information to also scale with temperature. To aid our cell tracking, we imaged embryos in a chamber at 18°C whereas the standard temperature for raising and staging zebrafish is 28.5°C (Kimmel et al., 1995). The effect

of temperature on the rate of development during somitogenesis has been quantified and using that information, we estimate that mechanical information would travel at a rate of 3 to 4 μm per min at 28.5°C (Schröter et al., 2008). With an average cell diameter of ~10 μm, the mechanical information passes from cell-to-cell in roughly 10 min at 18°C and in 2 to 3 min at 28.5°C. These rates are too rapid to be mediated via transcription and translation. Furthermore, the transcription factors most linked to mechanotransduction, Yap/Wwtr, function in the notochord and epidermis but not in the neural tube or paraxial mesoderm progenitors during zebrafish body elongation (Kimelman et al., 2017).

The mechanical information does not appear to propagate faster than morphogen diffusion (Müller et al., 2013). However, mechanical information could have a larger effective range as it may dissipate more slowly than the rate at which a morphogen concentration drops below a minimum threshold. Mechanical information may also more easily propagate anisotropically. For example, mechanical information may travel most effectively through a migrating population of cells. Since we only observe mechanical information as a disturbance in cell migration, we are tautologically unable to address this hypothesis. We are also not able to determine whether mechanical information travels downstream of the tail organizer into the PSM because the population of the PSM by *eve1* transgenic cells and other tail organizer cells makes it impossible to rule out cell-autonomous effects.

In summary, we find that an embryonic organizer orchestrates morphogenesis over distances beyond the range of morphogen signaling. This mechanical information is a secondary effect of canonical organizer cell signaling, and it is unclear whether it affects either gene expression or cell fate. Mechanical information is likely mediated by biochemical responses to cell-cell contact and not via force transfer between cells. Improved experimental methods for simultaneous spatiotemporal control of gene function and live imaging may reveal that mechanical information orchestrates morphogenesis in other contexts from embryonic development to organogenesis and regeneration.

STAR★METHODS

Detailed methods are provided in the online version of this paper and include the following:

- KEY RESOURCES TABLE
- CONTACT FOR REAGENT AND RESOURCE SHARING
- EXPERIMENTAL MODEL AND SUBJECT DETAILS
- METHOD DETAILS
  - Quantitative Real-Time PCR
  - Western Blot
  - In Situ Hybridization and Immunohistochemistry
  - Drug Treatment
  - Transgenic Embryos
  - Confocal Imaging
  - Image Analysis
  - Polarization (Quantification of global order)
  - Mean-Square Displacement (MSD)
  - Alignment Angle (Quantification of Local Order)
  - Top 10% Displacement Images
  - Simulation Methods

SUPPLEMENTAL INFORMATION

Supplemental Information can be found online at https://doi.org/10.1016/j.devcel.2019.05.014.

ACKNOWLEDGMENTS

We thank Miriam Genuth and Abdel-Rahman Hassan for comments on the manuscript and Josien van Wolfswinkel's lab for assistance with the qRT-PCR experiments. Research support provided by award R33GM114257 from the NIH Common Fund Single Cell Analysis Program to S.A.H., T.E., and C.S.O. and award 1R01GM129149-01 from NIGMS to S.A.H.

AUTHOR CONTRIBUTIONS

D.D. performed data analysis, the computational modeling with guidance from T.E., C.S.O., and M.D.S., and wrote the manuscript. D.J. and J.S.-S. performed the wet lab experiments, analyzed the data, and wrote the manuscript. A.K.L., N.D., and E.G. contributed to the wet lab experiments and data analysis. S.A.H. conceived of and directed the project and wrote the manuscript.

DECLARATION OF INTERESTS

The authors declare no competing interests.

Received: May 30, 2018
Revised: March 20, 2019
Accepted: May 3, 2019
Published: June 6, 2019

REFERENCES

Agathon, A., Thisse, C., and Thisse, B. (2003). The molecular nature of the zebrafish tail organizer. Nature *424*, 448–452.

Barone, V., Lang, M., Krens, S.F.G., Pradhan, S.J., Shamipour, S., Sako, K., Sikora, M., Guet, C.C., and Heisenberg, C.P. (2017). An effective feedback loop between cell-cell contact duration and morphogen signaling determines cell fate. Dev. Cell *43*, 198–211.e12.

Barro, O., Vriz, S., Joly, J.S., Joly, C., Condamine, H., and Boulekbache, H. (1995). Widespread expression of the eve1 gene in zebrafish embryos affects the anterior-posterior axis pattern. Dev. Genet. *17*, 117–128.

Beck, C.W., and Slack, J.M. (1999). A developmental pathway controlling outgrowth of the Xenopus tail bud. Development *126*, 1611–1620.

Beck, C.W., Whitman, M., and Slack, J.M. (2001). The role of BMP signaling in outgrowth and patterning of the Xenopus tail bud. Dev. Biol. *238*, 303–314.

Bénazéraf, B., Francois, P., Baker, R.E., Denans, N., Little, C.D., and Pourquié, O. (2010). A random cell motility gradient downstream of FGF controls elongation of an amniote embryo. Nature *466*, 248–252.

Boudet, J.F., Cassagne, J., and Kellay, H. (2009). Blast shocks in quasi-two-dimensional supersonic granular flows. Phys. Rev. Lett. *103*, 224501.

Brend, T., and Holley, S.A. (2009). Zebrafish whole mount high-resolution double fluorescent in situ hybridization. J. Vis. Exp. 1229.

Connors, S.A., Tucker, J.A., and Mullins, M.C. (2006). Temporal and spatial action of tolloid (mini fin) and chordin to pattern tail tissues. Dev. Biol. *293*, 191–202.

Cruz, C., Maegawa, S., Weinberg, E.S., Wilson, S.W., Dawid, I.B., and Kudoh, T. (2010). Induction and patterning of trunk and tail neural ectoderm by the homeobox gene eve1 in zebrafish embryos. Proc. Natl. Acad. Sci. USA *107*, 3564–3569.

Das, D., Chatti, V., Emonet, T., and Holley, S.A. (2017). Patterned disordered cell motion ensures vertebral column symmetry. Dev. Cell *42*, 170–180.e5.

Dray, N., Lawton, A.K., Nandi, A., Jülich, D., Emonet, T., and Holley, S.A. (2013). Cell-fibronectin interactions propel vertebrate trunk elongation via tissue mechanics. Curr. Biol. *23*, 1335–1341.

Dush, M.K., and Martin, G.R. (1992). Analysis of mouse Evx genes: Evx-1 displays graded expression in the primitive streak. Dev. Biol. *151*, 273–287.

Fainsod, A., Steinbeisser, H., and De Robertis, E.M. (1994). On the function of BMP-4 in patterning the marginal zone of the Xenopus embryo. EMBO J. *13*, 5015–5025.

Fior, R., Maxwell, A.A., Ma, T.P., Vezzaro, A., Moens, C.B., Amacher, S.L., Lewis, J., and Saúde, L. (2012). The differentiation and movement of presomitic mesoderm progenitor cells are controlled by Mesogenin 1. Development *139*, 4656–4665.

Fürthauer, M., Lin, W., Ang, S.L., Thisse, B., and Thisse, C. (2002). Sef is a feedback-induced antagonist of Ras/MAPK-mediated FGF signalling. Nat. Cell Biol. *4*, 170–174.

Gofflot, F., Hall, M., and Morriss-Kay, G.M. (1997). Genetic patterning of the developing mouse tail at the time of posterior neuropore closure. Dev. Dyn. *210*, 431–445.

Goldman, D.C., Martin, G.R., and Tam, P.P. (2000). Fate and function of the ventral ectodermal ridge during mouse tail development. Development *127*, 2113–2123.

Gönci, B., Nagy, M., and Vicsek, T. (2008). Phase transition in the scalar noise model of collective motion in three dimensions. Eur. Phys. J. Spec. Top. *157*, 53–59.

Goodwin, K., Ellis, S.J., Lostchuck, E., Zulueta-Coarasa, T., Fernandez-Gonzalez, R., and Tanentzapf, G. (2016). Basal cell-extracellular matrix adhesion regulates force transmission during tissue morphogenesis. Dev. Cell *39*, 611–625.

Goto, H., Kimmey, S.C., Row, R.H., Matus, D.Q., and Martin, B.L. (2017). FGF and canonical Wnt signaling cooperate to induce paraxial mesoderm from tailbud neuromesodermal progenitors through regulation of a two-step epithelial to mesenchymal transition. Development *144*, 1412–1424.

Gouti, M., Delile, J., Stamataki, D., Wymeersch, F.J., Huang, Y., Kleinjung, J., Wilson, V., and Briscoe, J. (2017). A gene regulatory network balances neural and mesoderm specification during vertebrate trunk development. Dev. Cell *41*, 243–261.

Hao, J., Ho, J.N., Lewis, J.A., Karim, K.A., Daniels, R.N., Gentry, P.R., Hopkins, C.R., Lindsley, C.W., and Hong, C.C. (2010). In vivo structure-activity relationship study of dorsomorphin analogues identifies selective VEGF and BMP inhibitors. ACS Chem. Biol. *5*, 245–253.

Heisenberg, C.P., and Bellaïche, Y. (2013). Forces in tissue morphogenesis and patterning. Cell *153*, 948–962.

Joly, J.S., Joly, C., Schulte-Merker, S., Boulekbache, H., and Condamine, H. (1993). The ventral and posterior expression of the zebrafish homeobox gene eve1 is perturbed in dorsalized and mutant embryos. Development *119*, 1261–1275.

Jülich, D., Cobb, G., Melo, A.M., McMillen, P., Lawton, A.K., Mochrie, S.G.J., Rhoades, E., and Holley, S.A. (2015). Cross-scale integrin regulation organizes ECM and tissue topology. Dev. Cell *34*, 33–44.

Jülich, D., Hwee Lim, C., Round, J., Nicolaije, C., Schroeder, J., Davies, A., Geisler, R., Lewis, J., Jiang, Y.J., Holley, S.A., et al. (2005). Beamter/deltaC and the role of Notch ligands in the zebrafish somite segmentation, hindbrain neurogenesis and hypochord differentiation. Dev. Biol. *286*, 391–404.

Kim, J.H., Lee, S.R., Li, L.H., Park, H.J., Park, J.H., Lee, K.Y., Kim, M.K., Shin, B.A., and Choi, S.Y. (2011). High cleavage efficiency of a 2A peptide derived from porcine teschovirus-1 in human cell lines, zebrafish and mice. PLoS ONE *6*, e18556.

Kimelman, D., Smith, N.L., Lai, J.K.H., and Stainier, D.Y. (2017). Regulation of posterior body and epidermal morphogenesis in zebrafish by localized Yap1 and Wwtr1. eLife *6*.

Kimmel, C.B., Ballard, W.W., Kimmel, S.R., Ullmann, K.S.B., and Schilling, T.F. (1995). Stages of embryonic development of the zebrafish. Dev. Dyn. *203*, 253–310.

Lander, A.D. (2007). Morpheus unbound: reimagining the morphogen gradient. Cell *128*, 245–256.

Lawton, A.K., Nandi, A., Stulberg, M.J., Dray, N., Sneddon, M.W., Pontius, W., Emonet, T., and Holley, S.A. (2013). Regulated tissue fluidity steers zebrafish body elongation. Development *140*, 573–582.

LeGoff, L., and Lecuit, T. (2015). Mechanical forces and growth in animal tissues. Cold Spring Harbor Perspect. Biol. *8*, a019232.

Li, C., and Manley, J.L. (1998). Even-skipped represses transcription by binding TATA binding protein and blocking the TFIID-TATA box interaction. Mol. Cell. Biol. *18*, 3771–3781.

Link, V., Shevchenko, A., and Heisenberg, C.P. (2006). Proteomics of early zebrafish embryos. BMC Dev. Biol. *6*, 1.

Lye, C.M., Blanchard, G.B., Naylor, H.W., Muresan, L., Huisken, J., Adams, R.J., and Sanson, B. (2015). Mechanical coupling between endoderm invagination and axis extension in Drosophila. PLoS Biol. *13*, e1002292.

Manning, A.J., and Kimelman, D. (2015). Tbx16 and Msgn1 are required to establish directional cell migration of zebrafish mesodermal progenitors. Dev. Biol. *406*, 172–185.

Mara, A., Schroeder, J., Chalouni, C., and Holley, S.A. (2007). Priming, initiation and synchronization of the segmentation clock by deltaD and deltaC. Nat. Cell Biol. *9*, 523–530.

Martin, B.L., and Kimelman, D. (2012). Canonical Wnt signaling dynamically controls multiple stem cell fate decisions during vertebrate body formation. Dev. Cell *22*, 223–232.

McKay, L.M., Carpenter, B., and Roberts, S.G. (1999). Evolutionary conserved mechanism of transcriptional repression by even-skipped. Nucleic Acids Res. *27*, 3064–3070.

McMillen, P., and Holley, S.A. (2015). The tissue mechanics of vertebrate body elongation and segmentation. Curr. Opin. Genet. Dev. *32*, 106–111.

Mongera, A., Rowghanian, P., Gustafson, H.J., Shelton, E., Kealhofer, D.A., Carn, E.K., Serwane, F., Lucio, A.A., Giammona, J., and Campàs, O. (2018). A fluid-to-solid jamming transition underlies vertebrate body axis elongation. Nature *561*, 401–405.

Monnier, N., Guo, S.M., Mori, M., He, J., Lénárt, P., and Bathe, M. (2012). Bayesian approach to MSD-based analysis of particle motion in live cells. Biophys. J. *103*, 616–626.

Müller, P., Rogers, K.W., Yu, S.R., Brand, M., and Schier, A.F. (2013). Morphogen transport. Development *140*, 1621–1638.

Mullins, M.C., Hammerschmidt, M., Kane, D.A., Odenthal, J., Brand, M., van Eeden, F.J.M., Furutani-Seiki, M., Granato, M., Haffter, P., Heisenberg, C.P., et al. (1996). Genes establishing dorsoventral pattern formation in the zebrafish embryo: the ventral specifying genes. Development *123*, 81–93.

C. Nüsslein-Volhard, and R. Dahm, eds. (2002). Zebrafish (Oxford University Press).

Ohta, S., Suzuki, K., Tachibana, K., Tanaka, H., and Yamada, G. (2007). Cessation of gastrulation is mediated by suppression of epithelial-mesenchymal transition at the ventral ectodermal ridge. Development *134*, 4315–4324.

O'Neill, K., and Thorpe, C. (2013). BMP signaling and spadetail regulate exit of muscle precursors from the zebrafish tailbud. Dev. Biol. *375*, 117–127.

Pourquié, O. (2011). Vertebrate segmentation: from cyclic gene networks to scoliosis. Cell *145*, 650–663.

Pyati, U.J., Webb, A.E., and Kimelman, D. (2005). Transgenic zebrafish reveal stage-specific roles for Bmp signaling in ventral and posterior mesoderm development. Development *132*, 2333–2343.

Rericha, E.C., Bizon, C., Shattuck, M.D., and Swinney, H.L. (2002). Shocks in supersonic sand. Phys. Rev. Lett. *88*, 014302.

Roszko, I., Sawada, A., and Solnica-Krezel, L. (2009). Regulation of convergence and extension movements during vertebrate gastrulation by the Wnt/PCP pathway. Semin. Cell Dev. Biol. *20*, 986–997.

Row, R.H., and Kimelman, D. (2009). Bmp inhibition is necessary for post-gastrulation patterning and morphogenesis of the zebrafish tailbud. Dev. Biol. *329*, 55–63.

Row, R.H., Pegg, A., Kinney, B.A., Farr, G.H., 3rd, Maves, L., Lowell, S., Wilson, V., and Martin, B.L. (2018). BMP and FGF signaling interact to pattern mesoderm by controlling basic helix-loop-helix transcription factor activity. eLife *7*.

Sawada, A., Shinya, M., Jiang, Y.J., Kawakami, A., Kuroiwa, A., and Takeda, H. (2001). Fgf/MAPK signalling is a crucial positional cue in somite boundary formation. Development *128*, 4873–4880.

Schröter, C., Herrgen, L., Cardona, A., Brouhard, G.J., Feldman, B., and Oates, A.C. (2008). Dynamics of zebrafish somitogenesis. Dev. Dyn. *237*, 545–553.

Seebald, J.L., and Szeto, D.P. (2011). Zebrafish eve1 regulates the lateral and ventral fates of mesodermal progenitor cells at the onset of gastrulation. Dev. Biol. *349*, 78–89.

Shyer, A.E., Huycke, T.R., Lee, C., Mahadevan, L., and Tabin, C.J. (2015). Bending gradients: how the intestinal stem cell gets its home. Cell *161*, 569–580.

Steventon, B., Duarte, F., Lagadec, R., Mazan, S., Nicolas, J.F., and Hirsinger, E. (2016). Species-specific contribution of volumetric growth and tissue convergence to posterior body elongation in vertebrates. Development *143*, 1732–1741.

Stickney, H.L., Imai, Y., Draper, B., Moens, C., and Talbot, W.S. (2007). Zebrafish bmp4 functions during late gastrulation to specify ventroposterior cell fates. Dev. Biol. *310*, 71–84.

Stulberg, M.J., Lin, A., Zhao, H., and Holley, S.A. (2012). Crosstalk between Fgf and Wnt signaling in the zebrafish tailbud. Dev. Biol. *369*, 298–307.

Szabó, B., Szöllösi, G.J., Gönci, B., Jurányi, Z., Selmeczi, D., and Vicsek, T. (2006). Phase transition in the collective migration of tissue cells: experiment and model. Phys. Rev. E Stat. Nonlin Soft Matter Phys. *74*, 061908.

Szeto, D.P., and Kimelman, D. (2004). Combinatorial gene regulation by Bmp and Wnt in zebrafish posterior mesoderm formation. Development *131*, 3751–3760.

Thisse, C., and Thisse, B. (2005) High throughput expression analysis of ZF-models consortium clones. ZFIN Direct Data Submission.

Weiser, D.C., Row, R.H., and Kimelman, D. (2009). Rho-regulated myosin phosphatase establishes the level of protrusive activity required for cell movements during zebrafish gastrulation. Development *136*, 2375–2384.

Williams, M.L., and Solnica-Krezel, L. (2017). Regulation of gastrulation movements by emergent cell and tissue interactions. Curr. Opin. Cell Biol. *48*, 33–39.

Wilson, C.A., High, S.K., McCluskey, B.M., Amores, A., Yan, Y.L., Titus, T.A., Anderson, J.L., Batzel, P., Carvan, M.J., 3rd, Schartl, M., et al. (2014). Wild sex in zebrafish: loss of the natural sex determinant in domesticated strains. Genetics *198*, 1291–1308.

Wilson, V., Olivera-Martinez, I., and Storey, K.G. (2009). Stem cells, signals and vertebrate body axis extension. Development *136*, 1591–1604.

Xiong, F., Tentner, A.R., Huang, P., Gelas, A., Mosaliganti, K.R., Souhait, L., Rannou, N., Swinburne, I.A., Obholzer, N.D., Cowgill, P.D., et al. (2013). Specified neural progenitors sort to form sharp domains after noisy Shh signaling. Cell *153*, 550–561.

Yang, Y., and Thorpe, C. (2011). BMP and non-canonical Wnt signaling are required for inhibition of secondary tail formation in zebrafish. Development *138*, 2601–2611.

STAR★METHODS

KEY RESOURCES TABLE

REAGENT or RESOURCE	SOURCE	IDENTIFIER
Antibodies		
Rabbit anti-pSMAD1/5/8 primary antibody	Cell Signaling Technologies	mAb #9516; RRID: AB_491015
Rabbit anti-H2B	Abcam	ab1790; RRID: AB_302612
Goat anti-rabbit HRP	ThermoFisher	G-21234; RRID: AB_1500696
Chemicals, Peptides, and Recombinant Proteins		
DMH1	Tocris Biosciences	Cat#4126
Critical Commercial Assays		
RNeasy Micro Kit	Qiagen	Cat#74004
Applied Biosystems High-Capacity cDNA RT Kit	ThermoFisher	Cat# 4368814
Thermo Scientific Pierce ECL 2 Western Blotting Substrate	ThermoFisher	Cat#PI80196
Experimental Models: Organisms/Strains		
Danio rerio: Strain TL	ZIRC	ZL86
Danio rerio: Strain TU	ZIRC	ZL57
Danio rerio: Strain AB	ZIRC	ZL1
Oligonucleotides		
See Table S1 for qPCR Primers		N/A
Recombinant DNA		
Plasmid: pT2 tbx6l-βglobin:eve1-P2A-emGFP	This paper	N/A
Plasmid: pT2 tbx6l-βglobin:cpi17-P2A-emGFP	This paper	N/A
Plasmid: pT2 tbx6l-βglobin:emGFP	This paper	N/A
Software and Algorithms		
Imaris	Bitplane	N/A
Matlab	MathWorks	N/A
Code for modeling tailbud cell motion in 3D	https://github.com/emonetlab/Mechanical-Information-Propagation	N/A
Other		
Zeiss LSM 510	Zeiss	N/A
Zeiss Plan-Apochromat 20x, W = 0.8 NA	Zeiss	N/A
Zeiss Axioskop 2	Zeiss	N/A
Zeiss FLUAR 5x, 0.25 NA	Zeiss	N/A

CONTACT FOR REAGENT AND RESOURCE SHARING

Further information and requests for resources and reagents should be directed to and will be fulfilled by the Lead Contact, Scott Holley (scott.holley@yale.edu).

EXPERIMENTAL MODEL AND SUBJECT DETAILS

Zebrafish care and breeding followed standard protocols (Nüsslein-Volhard and Dahm, 2002) as approved by Yale IACUC. Briefly, zebrafish are housed in a recirculating tank system. Embryos are attained from adults placed pairwise in mating tanks for natural spawning. Adults are returned to their regular tanks after mating and given at least two weeks before the next mating. Wild-type strains used for morphological and qPCR analyses were Tübingen and for imaging and western blots were TL and TLAB. For all assays, embryos were raised at 28°C for 2 h, followed by 22°C for 11 h and then 20°C until treatment. All experiments are performed on embryos within the first 48 h of development well before sex determination in zebrafish (Wilson et al., 2014).

METHOD DETAILS

Quantitative Real-Time PCR

Embryos were treated with 40 μM DMH1 or 0.4% DMSO vehicle control at approximately the 5-somite stage (5ss) for 1, 3, or 5 h. Embryos were manually dissected to isolate the presomitic mesoderm in Mark's Modified Ringer buffer with 10 mM HEPES. Approximately 50 tailbuds were pooled per experimental replicate. RNA was extracted using the RNeasy Micro Kit (Qiagen) and cDNA was reverse transcribed using the High-Capacity cDNA RT kit (Applied Biosystems/ThermoFisher). qRT-PCR was performed as previously described (Stulberg et al., 2012). cDNA was mixed with primers, buffer, and power SYBR green (Applied Biosystems) and loaded in a 7900 HT Applied Biosystems machine. Cycle parameters were 95°C for 10 min, followed by 40 cycles of 95°C for 10 s, 58°C for 1 min. Primer concentrations were adjusted to attain primer efficiencies between 90%–120%. The *Tg cpi-17* experiments were performed on a QuantStudio3 (Applied Biosystems). Three replicates were performed for all measurements. Primer sequences are provided in Table S1. Most primers were designed to include one exonic and one intronic sequence, so only nascent transcripts were measured. When intronic primers were unavailable, both primers were in exonic regions. Fold change was calculated as $2^{-\Delta\Delta C_t}$, where expression was normalized to β-actin and compared to a control, and converted to $\log_{10}$. Statistical comparisons were made using the Student's unpaired *t* test.

Western Blot

Embryos were treated at the 5-somite stage with 40 μM DMH1 or 0.4% DMSO for 3 h. Embryos were manually dissected in Mark's Modified Ringer with 10 mM HEPES, and tissue was deyolked and protein extracted as in (Link et al., 2006). Protein samples were run on a 12% SDS-PAGE gel at 200V for 90 min. After blocking with 5% milk in TBST, blots were incubated two nights in 1:500 α-pSmad1/5/8 (Cell Signaling Technologies) at 4°C in block. Next, blots were rinsed twice in TBST, washed 1× 10 min and 3× 5 min before incubating for 90 min in 1:10,000 α-H2B (Abcam) in block. Blot was washed in TBST as before and incubated 1:50,000 in goat α-rabbit HRP (Sigma-Aldrich) for 2 h before a third wash procedure and detection with Pierce ECL 2 (Thermo Scientific). Western blots were visualized using a Typhoon FLA 9500 Phosphorimager (GE) and quantified using ImageQuant software.

In Situ Hybridization and Immunohistochemistry

For immunohistochemistry, embryos were stained using anti-pSMAD1/5/8 primary antibody (Cell Signaling Technologies) at a concentration of 1:100, and the endogenous GFP signal was used to identify transgenic cells. Shown are heat maps of a single representative 1.2-μm optical slice of pSMAD1/5/8 staining with GFP-positive cells circled in white. Double fluorescent in situ hybridization for *eve1* and *bmp4* was performed as previously described (Brend and Holley, 2009; Jülich et al., 2005). Probes were amplified by PCR from wild-type cDNA. Primers used were eve1F: tggcttggaagagaaacagtgacg, eve1R+T7: aatacgactcactatagtcaggtctggaatga cacaggagt, bmp4F: atgattcctggtaatcgaatg and bmp4R+T7: cgtaatacgactcactatagggttagcggcagccacacccctc. Shown is projection view of z-stack from a representative embryo. Images were taken with a Zeiss 510 LSM confocal microscope. Three experimental replicates were performed for each assay with a total of twelve embryos imaged for GFP/pSMAD1 antibody stains, and ten embryos for *eve1/bmp4* in situs.

Drug Treatment

Embryos were treated at the 5-somite stage with 40 μM DMH1 or 0.4% DMSO. DMH1 was dissolved in DMSO to a stock concentration of 10 mM, and further diluted in E2 for treatment. Embryos were dechorionated with pronase and kept at 28°C after treatment. Morphological analysis was performed using a dissecting microscope at both 5 and 24 h post treatment.

Transgenic Embryos

Embryos were injected with 30 ng/μl *pT2 tbx6l-βglobin:eve1-P2A-emGFP* DNA and 150-ng/μl *transposase* mRNA, 150 ng/μl *pT2 tbx6l-βglobin:cpi17-P2A-emGFP* DNA and 50-ng/μl *transposase* mRNA or 150 ng/μl *pT2 tbx6l-βglobin:emGFP* DNA and 50-ng/μl *transposase* mRNA at the 1-cell stage and raised as described above. The tbx6l enhancer drives transcription in the posterior tailbud (Dray et al., 2013; Jülich et al., 2015; Szeto and Kimelman, 2004). The 5′ UTR of human beta globin was used to increase translation. The P2A sequence enabled expression of two peptides from a single mRNA (Kim et al., 2011). Embryos were manually sorted for strong GFP fluorescence in the tail between the tailbud and 5-somite stage using a fluorescent dissecting microscope.

Confocal Imaging

Embryos were injected with 100 ng/μl nls-RFP mRNA at the 1-cell stage and raised as above. Embryos were mounted on their tail in 1.5% low-melt agarose on a 24x50mm coverslip (FisherScientific), and chambers were backfilled with DMH1 or DMSO solution. Videos were taken at 18°C using a Linkam Scientific PE100 cooling stage on a Zeiss LSM 510 confocal microscope for 1.5 to 3 h. Cell movement was tracked and manually sorted based on tailbud region (PNT, DM, TO/PZ, PSM) using Imaris software (Bitplane) as previously described (Lawton et al., 2013).

Image Analysis

Distributions for cell track straightness, mean coefficient of variation (C.V.) of cell track speed and track mean speed for all cells within each region (PNT, DM, TO/PZ, PSM) were exported directly from Imaris. Average values for each region are shown, but statistical

tests were based on the full distribution using ANOVA analysis with bootstrapping. The data extracted from Imaris were analyzed to calculate the polarization, MSD, local order, distribution of nearest neighbors, and probability of negative V_y. For the calculations of these quantities, we used the center of mass of the anterior 50 μm of the PSM as our reference frame to correct for global growth of the embryo as described previously (Lawton et al., 2013). The individual cell positions and velocities were then corrected as below:

$$\vec{r}_i = \vec{r}_i^{IMARIS} - \vec{V}_{CM}^{APSM}\Delta t, \quad \vec{v}_i = \vec{v}_i^{IMARIS} - \vec{V}_{CM}^{APSM}.$$

Here $\vec{r}_i^{IMARIS}$ and $\vec{v}_i^{IMARIS}$ are the instantaneous individual positions and velocities respectively extracted from Imaris (raw data); $\vec{r}_i$ and $\vec{v}_i$ are the corrected instantaneous positions and velocities respectively; $\vec{V}_{CM}^{APSM}$ is the velocity of the center of mass of the anterior 50 μm of the PSM; and Δt is the time step (Δt is about 3 min in the experimental videos). All quantities were calculated using custom codes written in Matlab, and are defined below.

Polarization (Quantification of global order)

The polarization is defined as:

$$\Phi = \left\langle \left| (1/N)\sum_{i=1}^{N} (\vec{v}_i/|\vec{v}_i|) \right| \right\rangle.$$

Here, the summation indicates an average taken over the total number of cells (N) at each time point, and the outer brackets indicate an average over all time points. For high global order, Φ is close to 1, and for global disorder Φ is close to 0.

Mean-Square Displacement (MSD)

The MSD for each individual track is defined by $\langle(\vec{r}_i(t+\tau) - \vec{r}_i(t))^2\rangle$, where τ is the lag-time. Diffusion and velocity coefficients for each tailbud region were calculated as before (Dray et al., 2013) by utilizing a Bayesian approach to select the most appropriate model (Monnier et al., 2012). The best-fitted model was a drift-diffusive motion for all the experimental videos.

Alignment Angle (Quantification of Local Order)

For each *i*-th cell, we defined the 'alignment angle' as $\theta_i = \cos^{-1}[(\vec{v}_i/|\vec{v}_i|)\cdot(\vec{V}_i/|\vec{V}_i|)]$. Here, $\vec{V}_i$ denotes a local mean velocity averaged over the cells (including cell *i*) that lie within a sphere of 20 μm radius, centering on cell *i*. For high local order, there is a greater probability of θ_i to be close to zero.

Top 10% Displacement Images

We previously found that patterns of cell flow in the tail organizer can be visualized by displaying only the top 10% of cell tracks with the greatest displacement in a given direction (Lawton et al., 2013). To create the top 10% displacement images, the top 10% of cell tracks displacing ventrally within the PZ were selected and subsequently deleted from the region before selecting and deleting the top 10% of tracks that displaced laterally, then anteriorly, and finally in the dorsal direction so as to ensure no tracks were double-counted. Selected tracks were color-coded and grouped together for visualization.

Simulation Methods

Based on our previous 2D model of tailbud cell migration (Das et al., 2017), we developed a more realistic 3D model of zebrafish tail elongation. Each cell, *i*, is modeled as a self-propelled soft particle with a radius a_i and instantaneous position $\vec{r}_i$, which moves with a constant self-propelling speed v_0 in a well-defined direction $\hat{n}_i$. In the overdamped limit (i.e. when cell inertia is negligible), the dynamics of the *i*-th cell is given by

$$\frac{d\vec{r}_i}{dt} = v_0\hat{n}_i + \mu\sum_j \vec{f}(\vec{r}_i, \vec{r}_j). \qquad \text{(Equation 1)}$$

Here, μ is the mobility parameter, and $\vec{f}(\vec{r}_i, \vec{r}_j)$ is an intercellular force between the *i*-th and *j*-th cells. The intercellular force is summed over all the nearest neighbors. Thus, the instantaneous velocity of each individual cell ($d\vec{r}_i/dt = \dot{\vec{r}}_i$) is determined by two distinct factors: one is the cellular self-propelling velocity ($v_0\hat{n}_i$) stemming from an active force, and the other is the net intercellular force exerted by its neighbors.

To model the emergence of collective order, we combined the essential feature of local velocity alignment of individual cells from a 2D model (Szabó et al., 2006) with a 3D Vicsek model (Gönci et al., 2008). The direction of cellular self-propulsion ($\hat{n}_i$) attempts to align itself to the direction of the instantaneous velocity ($\hat{r}_i = \dot{\vec{r}}_i/|\dot{\vec{r}}_i|$), but with some uncertainty. The self-propelling directions of the cells were updated following the rule

$$\hat{n}_i(t+\Delta t) = R(\hat{e},\xi)\cdot\hat{r}_i(t)\xi. \qquad \text{(Equation 2)}$$

Here Δt is the time step, set at $\Delta t = 0.005$ in the simulations. $R(\hat{e},\xi)$ is a rotation matrix that represents a random rotation of the instantaneous direction of individual velocity ($\hat{r}_i$) about a random axis (defined by the unit vector $\hat{e}$), and by a random angle, ξ. The unit vector

$\hat{e}$ is a random vector perpendicular to $\hat{r}_i$, and chosen from a uniform distribution. Thus, $\hat{e}$ defines a random axis for the rotation. The random angle, ξ represents the 'angular noise', which is a random number chosen uniformly in the interval $\eta[-\pi,\pi]$, where η is the strength of the angular noise. The value of η varies from 0 to 1. When the angular noise strength is zero ($\eta = 0$), ordered motion quickly emerges. At maximum noise ($\eta = 1$), the motion is completely random.

The intercellular force is modeled as a short-ranged and piece-wise linear function of intercellular distance $r_{ij} = |\vec{r}_i - \vec{r}_j|$. This force is repulsive for distances smaller than R_{eq}, while it is attractive for distances $R_{eq} \leq r_{ij} \leq R_0$, and zero if cells are farther apart than R_0:

$$\vec{f}(\vec{r}_i, \vec{r}_j) = \hat{r}_{ij} f_{rep} \frac{(R_{eq} - r_{ij})}{R_{eq}}, \quad r_{ij} < R_{eq}$$
$$= \hat{r}_{ij} f_{adh} \frac{(R_{eq} - r_{ij})}{(R_0 - R_{eq})} \quad R_{eq} \leq r_{ij} \leq R_0 \qquad \text{(Equation 3)}$$
$$= 0, \quad r_{ij} > R_0$$

Here, f_{rep} and f_{adh} are the maximum repulsive and adhesive forces, and $\hat{r}_{ij} = (\vec{r}_i - \vec{r}_j)/|\vec{r}_i - \vec{r}_j|$. Note that repulsive forces in the simulation may represent a number of in vivo mechanisms including volume exclusion between cells, as two cells cannot occupy the same space as well as biochemical processes such as contact mediated repulsion. The adhesive forces result from cell-cell attractive interactions mediated by proteins like Cadherins. We set $f_{rep} >> f_{adh}$ to avoid any clustering (or crystallization) of cells, which was never observed experimentally. The equilibrium distance between two cells (i and j) is taken to be $R_{eq} = (a_i + a_j)$, i.e. the sum of the corresponding radii. We assigned the individual cellular radii within the range $a_i \in [a_0 - \delta, a_0 + \delta]$, i.e. uniformly distributed about the average radius a_0 with root-mean-square fluctuations ($\delta = 0.05$).

We simulated the cell motion by numerically integrating Equations 1 and 2 using the 'explicit Euler' method with a time step $\Delta t = 0.005$, and assuming a perfectly reflecting boundary condition (rigid boundaries). We start with random initial positions and self-propulsion directions of the cells. The cells are initialized at a high packing fraction (0.95), as cells are closely packed inside the tailbud. The shape of the tailbud is modeled as a half-cylindrical structure, and its medial-lateral (ML) dimension matches that of the experimental datasets (see Figure S4A). The ML dimension of the tailbud is roughly $L_0/2a_0 \approx 12$ cells wide, while the width of the PSM is about half of the PNT (Figure S4A). Here L_0 is the ML width of the tailbud and a_0 is the average cell radius. We set $L_0 = 10$ and $2a_0 = 5/6$ in the simulations.

To make the tailbud grow in time, cells were introduced in the PNT at a constant rate from the anterior boundary (Figure S4A). This approximates the posterior flow of cells in the embryo partly due to convergent extension (Roszko et al., 2009; Steventon et al., 2016). We introduce a cell in every γ iteration steps, where γ is a parameter that controls the cell influx. In response to the increase in cell number in the PNT, we simultaneously slide the curved posterior boundary and the boundary separating left and right PSMs in the posterior direction (see the bold red arrows in Figure S4A). The barrier between PNT and PSM represents the ECM that progressively forms over time and binds the cells to the epidermis. To estimate the increase in the anterio-posterior (AP) length of the half-cylindrical structure, we assumed that the global cell density is constant, i.e.

$$\frac{N(t)}{V(t)} = \frac{N(t+\Delta t)}{V(t+\Delta t)} \quad or, \quad \Delta V = \Delta N \frac{V(t)}{N(t)}. \qquad \text{(Equation 4)}$$

Here, $N(t)$ is the total cell number inside the tailbud, and $V(t)$ is the net volume of the half-cylindrical tailbud at an instant, t. Thus, the increase in volume $\Delta V = V(t+\Delta t) - V(t)$ can be calculated from the increase in cell number $\Delta N = N(t+\Delta t) - N(t)$. From geometrical consideration, the total volume of the tailbud at any instant is given by

$$V(t) = \frac{1}{2}\pi (L_0/2)^2 L_{PSM}(t) + \frac{1}{4}\left(\frac{4}{3}\pi (L_0/2)^3\right). \qquad \text{(Equation 5)}$$

Here, L_{PSM} is the instantaneous AP length of the PSM (Note that the length of PNT is the same as the length of PSM in our model, see Figure S2A). So the overall AP length of the tailbud is $L_{tot} = L_{PSM} + L_{TO}$. The length of the tail-organizer, L_{TO} is kept fixed over time; while the length of the PSM (L_{PSM}) and consequently the total length (L_{tot}) increase over time as below

$$L_{tot}(t+\Delta t) = L_{tot}(t) + \Delta L, \quad and \quad L_{PSM}(t+\Delta t) = L_{PSM}(t) + \Delta L. \qquad \text{(Equation 6)}$$

Here, ΔL is the length increment at each time step, by which amount the boundaries need to be moved posteriorly, preserving the shape of the half-cylindrical structure (see Figure S2A). The length increment ΔL is calculated by simultaneously solving Equations 4 and 5 at each time step.

Parameters Values

To simulate the wild-type cell motion, we used $v_0 = 1$, $\mu = 1$, $\gamma = 5$, $\eta = 0.7$, $f_{adh} = 1$, $f_{rep} = 30$, and $R_0 = 1.2R_{eq}$, consistent with our earlier 2D model (Das et al., 2017). This set of parameters mimics the observed wild-type cell motion in the PNT, and correctly reproduces the wild-type value of polarization.

Numerical Rules to Introduce Perturbation in the Tail Organizer

To introduce a local perturbation in the tail-organizer (TO), we stochastically increased the cell repulsion of a group of cells that migrate into the TO after an onset of the perturbation. Each cell that migrates into the TO from the DM has a given probability of

80% to increase its repulsion parameter value, and any cell that comes into contact with this 'perturbed' cell, experiences a higher cell-cell repulsion. Once a cell switches to a higher value of the repulsion parameter, it cannot return to the 'wild-type' state again. Thus, the perturbation creates a continuous pool of cells with high repulsion in the TO. The enhanced value of the repulsion is 7 times the wild-type value ($f_{purt} = 7f_{rep}$).

Analysis of the Simulation Data

The codes for the model simulations were written in FORTRAN 90. The outputs of the program were averaged over 30 simulations of the tailbud in perturbed and in unperturbed conditions for data shown in Figure 4.

Analysis of Front Propagation in the Simulations

In the simulations, we quantified the response in cell motion in the PNT following a perturbation in the TO (Figures S4D–S4F). We quantified the net AP velocity in the PNT, V_y (defined as: $V_y = (\sum_{i=1}^{N} v_i^y)/N$ PNT, where v_i^y is the instantaneous y-component of the i-th cell, and N is the instantaneous number of cells in a box of fixed volume in the PNT). This AP velocity frequently becomes negative after the perturbation (Figure S4D). We also found that the cell density in the PNT increases after the perturbation (Figure S4E). Finally, the polarization sharply drops once the perturbation is switched on (Figure S4F).

To quantify the propagation of the disturbance created by the perturbation, we partitioned the PNT into a number of boxes with equal size starting from the posterior end of the PNT, and measured the spatial average of the net AP velocity $\langle V_y \rangle$ in each box, and plotted $\langle V_y \rangle$ as a function of the distance from the posterior end of PNT. In this velocity profile, the average AP velocity has both positive and negative parts (Figure S2E) and the zero-crossing point (black arrow heads in Figure S4G) progressively shifts towards the anterior. The zero-crossing point of $\langle V_y \rangle$ represents the front position at any instant (Cartoon below Figure S4G). A similar analysis for the density profile showed that the density has a peak near the posterior end, and this peak position slowly shifts towards the anterior with time (Figure S4H). To see how quickly the front propagates, we plotted the front position as a function of the elapsed time from the onset of the perturbation (Figure S4I). After a sharp initial rise, the front propagates almost linearly in time, and then damps out.

Significance Test

To establish if there is any significant difference between samples for a given quantity, we used a two-sample T-test provided by the MATLAB function 'ttest2'. Significance was defined as $p < 0.05$.

Developmental Cell, Volume *49*

Supplemental Information

Organization of Embryonic Morphogenesis via Mechanical Information

Dipjyoti Das, Dörthe Jülich, Jamie Schwendinger-Schreck, Emilie Guillon, Andrew K. Lawton, Nicolas Dray, Thierry Emonet, Corey S. O'Hern, Mark D. Shattuck, and Scott A. Holley

Supplemental Information

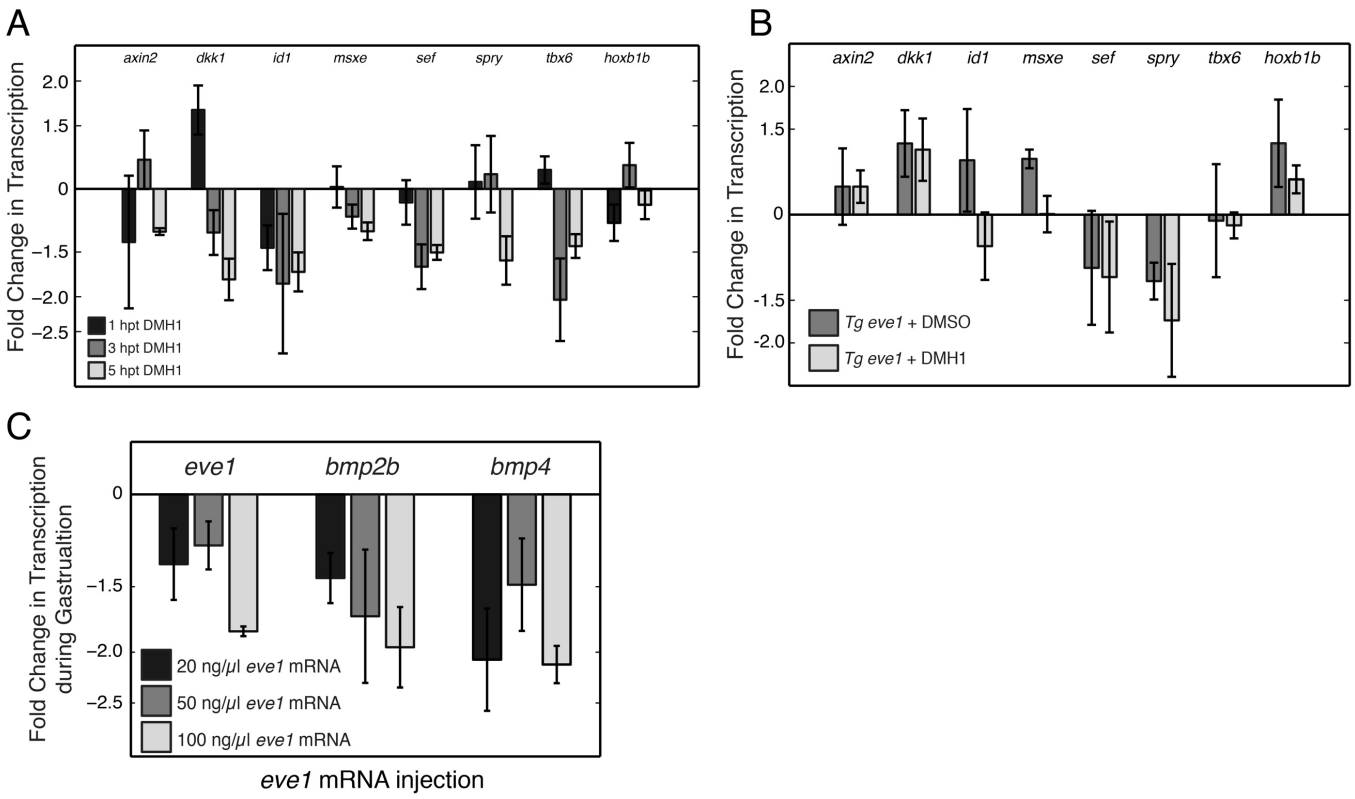

Figure S1. Effects of perturbation of tail organizer signaling on tailbud gene expression and Wnt and Fgf signaling. **Related to Figure 2.** Nascent transcription was measured by pRT-PCR on pooled dissected tailbuds. We quantified the expression of the Wnt target genes (*axin2*, *dkk1*), the Bmp target genes (*id1*, *msxe*), the Fgf target genes (*sef*, *spry*), and two genes expressed in the tailbud mesoderm, *tbx6l* and *hoxb1b*. Expression of all genes is normalized to *β-actin*. Data are averages from 3 independent experiments. Error bars represent the standard error. **(A)** A time-course of effects on gene expression after initiation of DMH1 treatment (hours post treatment: hpt). Expression was normalized to wild-type controls. Note that transcription of the canonical Bmp target *id1* is affected less severely than transcription of *eve1* and *bmp4* (Figure 2). **(B)** Gene expression in *Tg eve1* + DMSO tailbuds were compared to gene expression in *Tg eve1* + DMH1 tailbuds. Expression of Wnt and Fgf gene are the same in the conditions while expression of Bmp targets differ as shown for *eve1*, *bmp4* and pSMAD levels (Figure 2). Therefore, changes in Wnt or Fgf signaling cannot account for the stronger long-range effects in the PNT of *Tg eve1* + DMH1 embryos. **(C)** *eve1* over-expression represses *eve1*, *bmp4* and *bmp2b* transcription during gastrulation. mRNA encoding *eve1-2A-emGFP* was injected into one cell stage embryos at three different concentrations. RNA was isolated from 15-20 pooled embryos at 80% epiboly with three experimental replicates for each experimental condition. RT-qPCR quantified the fold change in the level of nascent transcription of *eve1*, *bmp2b* and *bmp4* compared to wild-type controls.

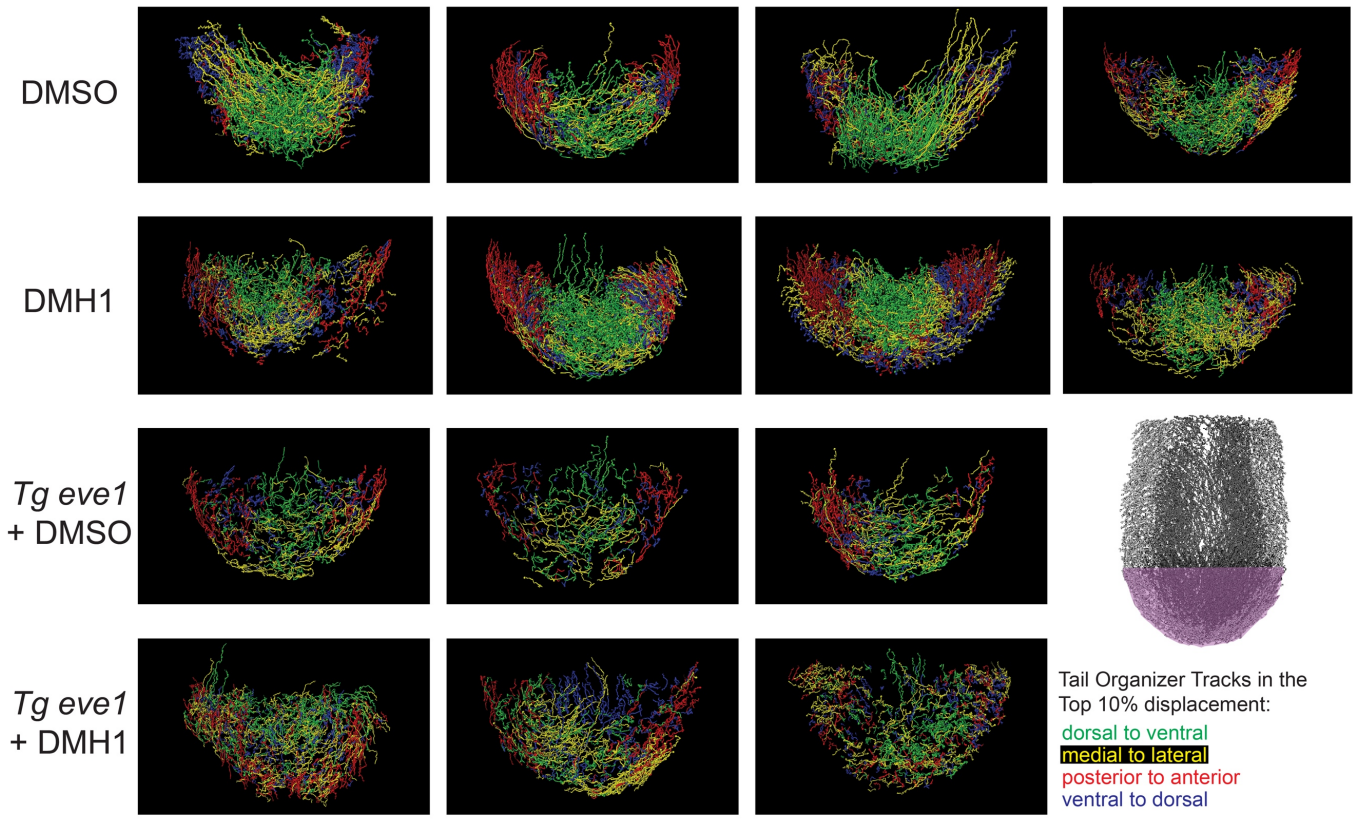

Figure S2. Disruption of cell flow through the tail organizer. Related to Figure 3. The lower right panel is the key indicating the position of the tail organizer (purple) and the color-coding scheme for the cell tracks. All other panels show cell tracks within the top 10% of all tracks in displacement from dorsal to ventral (green), medial to lateral (yellow), posterior to anterior (red) and ventral to dorsal (blue). Cell flow in the tail organizer is shown for four DMSO-treated control embryos, four DMH1-treated embryos, three *Tg tbx6l*:*eve1* transgenic DMSO-treated embryos and three *Tg tbx6l*:*eve1* transgenic DMH1-treated embryos. In DMSO control embryos, the dorsal to ventral flow is concentrated medially while the posterior to anterior and ventral to dorsal flows are concentrated laterally. This represents the predominant pattern of cell flow through the tail organizer. In experimental embryos, these flows are less well segregated indicating a more disordered flux through the tail organizer, particularly in *Tg eve1* + DMH1 embryos.

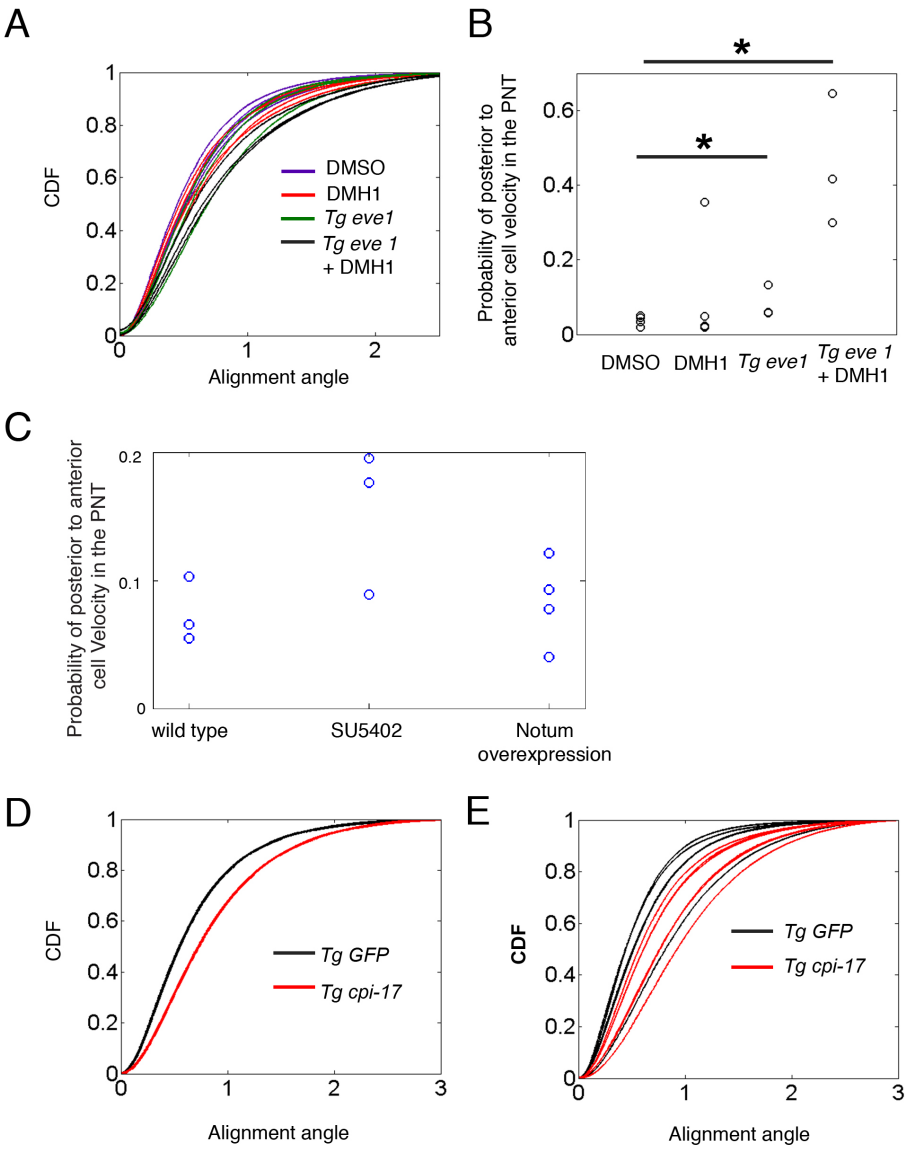

Figure S3. Experimental data for local order and probability of posterior to anterior velocities in the PNT. Related to Figures 4 and 6. (A) Local order in cell motion in the PNT is displayed via cumulative distribution functions (CDF) of alignment angles for each individual embryo (corresponding aggregate data shown in Figure 3E). The CDFs for DMSO-treated controls and *Tg eve1* + DMH1 embryos differ ($p<0.05$, t-test). **(B)** Changes in the probability of posterior to anterior cell velocity in the PNT in *Tg eve1* and *Tg eve1* + DMH1 embryos. Asterisks denote $p<0.05$ (t-test). **(C)** There is no change in the probability of posterior to anterior cell velocity in the PNT of SU5402 and notum1a overexpressing embryos. Note that *Tg eve1* + DMH1 average a probability of posterior to anterior cell velocities of over 0.4 (B). **(D)** Local order of cell motion in the PNT was quantified using a CDF of alignment angle for neighboring cell velocities. Local order in *Tg GFP* controls and *Tg cpi-17* embryos differ ($p<0.05$, t-test). Each distribution is obtained by pooling the data from each embryo into a single group. **(E)** CDF of alignment angles for each individual embryo in D.

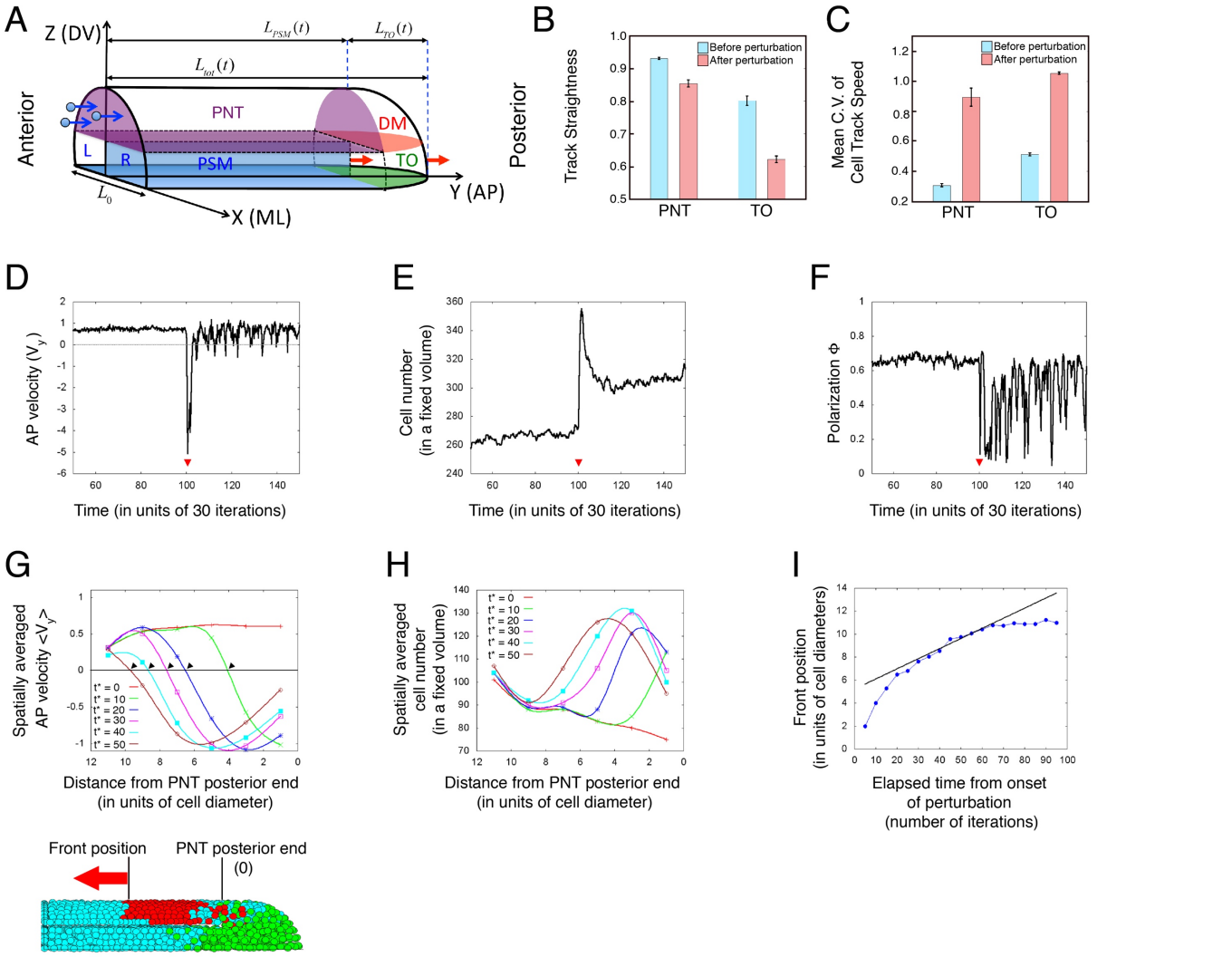

Figure S4. A 3D model of tailbud elongation. **Related to Figure 4.** Different tailbud domains are shown corresponding to Figure 1A. 'L' and 'R' denote the left and right sides of the PSM. The notochord is represented as a boundary between the left and right PSM. The anterior-posterior (AP) lengths of the PSM (L_{PSM}) and TO (L_{TO}), and the medial-lateral (ML) width of the tailbud (L_0) are also shown. Here X, Y and Z-axes represent the ML, AP, and dorsal-ventral (DV) axes, respectively. Cells are constantly added to the anterior end of the PNT. The anterior-posterior length of the tailbud, notochord and PSM incrementally increase at each time step (red arrows). **(B)** Cell track straightness in the PNT and TO is reduced after perturbation. **(C)** The mean C.V. of cell track speed is increased in both the PNT and TO after perturbation. **(D)** Net AP velocity, **(E)** cell number and **(F)** Polarization Φ within a fixed volume in the PNT are plotted against the simulation time. These figures show the responses in these quantities following a perturbation in the TO. Red arrowheads mark the onset of perturbation (See Movie S1). **(G)** Spatially averaged AP velocity and **(H)** spatially averaged cell number (in fixed volumes of equal sizes) as functions of the distance from the posterior end of the PNT. Here t* denotes the elapsed time from the onset of perturbation (at the onset of perturbation t*=0). Black arrowheads in E show the positions of the anteriorly propagating front (red arrow in the tailbud model below) relative to the posterior end of the PNT at each instant, t*. **(I)** Front position is plotted versus elapsed time from the onset of perturbation. The black straight line represents a linear speed of propagation, fitted for an intermediate time-regime (before the propagation damps out and leaving aside the initial transient-regime).

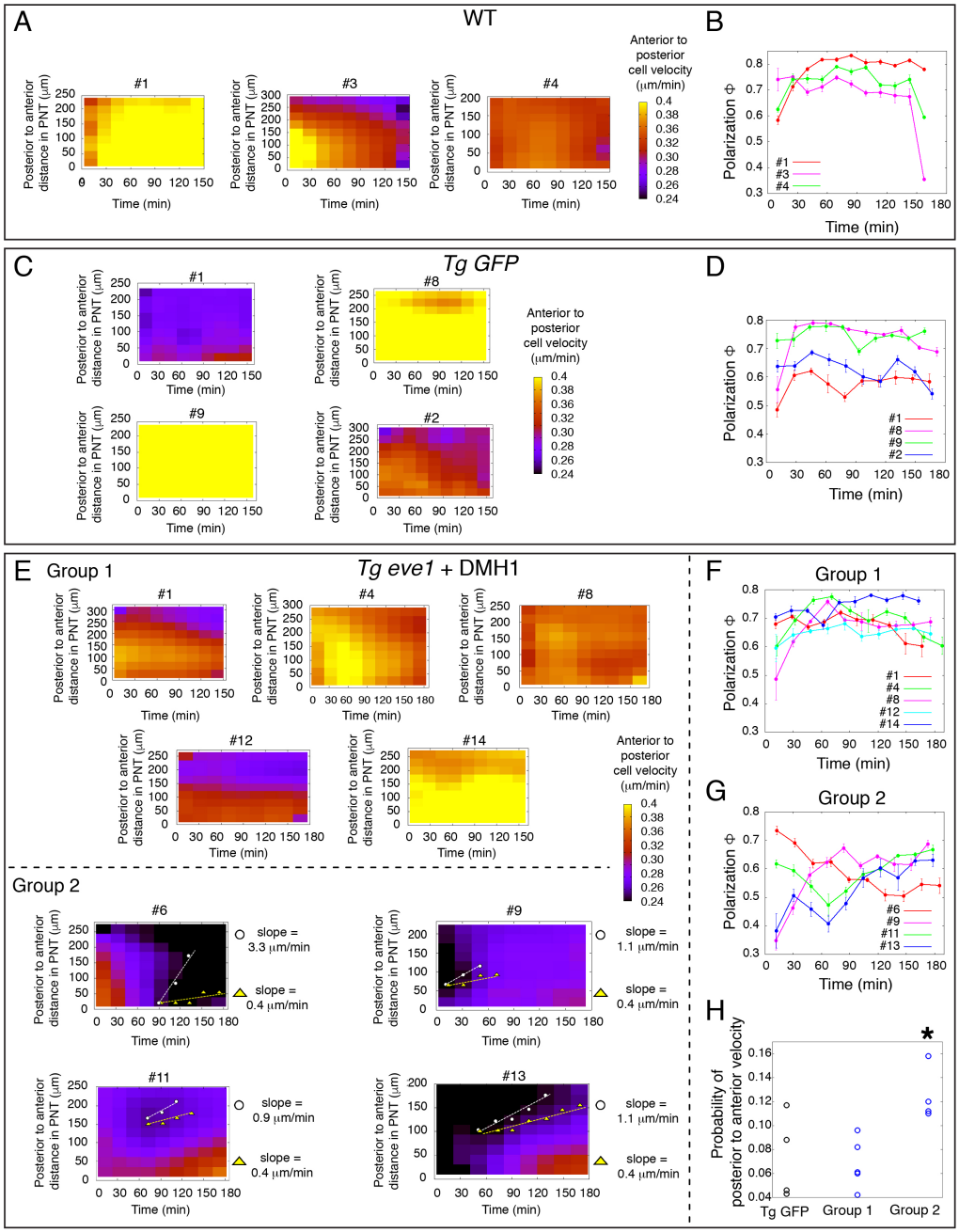

Figure S5. Estimating the rate of mechanical information in vivo. Related to Figure 5. (A) Heat maps plot the mean anterior to posterior cell velocity as a function of posterior to anterior distance along the PNT and time. Wild-type heat maps are relatively uniform. **(B)** Global order of cell motion (Polarization, Φ) was plotted as a function of time. The uniform wild-type heat maps are reflected in the high and relatively stable global order in the PNT of wild-type embryos. **(C)** *Tg tbx6l:GFP* control embryos produce heat maps that are relatively uniform. **(D)** Polarization in *Tg tbx6l:GFP* control embryos is high and stable over time. **(E)** *Tg tbx6l:eve1-GFP* embryos treated with DMH1 at the onset of imaging exhibit heterogenous heat maps. These embryos can be divided into two groups. Group 1 embryos resemble controls both in their heat maps and in their high and stable levels of global order (Polarization, Φ) **(F)**. Group 2 embryos exhibit disturbances in mean velocity that propagate from posterior to anterior in the PNT in their heat maps. We estimated the maximum and minimum slopes of the propagation of these disturbances. Group 2 embryos also display reduced and variable global order (Polarization, Φ) over time **(G)**. **(H)** Group 2 *Tg tbx6l:eve1-GFP* embryos exhibit an increase in the probability of posterior to anterior cell velocity in the PNT compared to Group 1 *Tg tbx6l:eve1-GFP* embryos and *Tg tbx6l:GFP* transgenic controls. Asterisk denotes $p<0.05$ (t-test).

Table S1. qPCR Primer sequences, Related to STAR Methods.

qPCR Primers	Sequence	Reference	Exon/Intron
bactin F	CGC GCA GGA GAT GGG AAC C	(Keegan et al., 2002)	Exon
bactin R	CAA CGG AAA CGC TCA TTG C	(Keegan et al., 2002)	Exon
axin2 F	GCG CGC ACA AAG TAG ACG TA	(Stulberg et al., 2012)	Intron
axin2 R	CCA GCA GCA AAG CCT TCA GT	(Stulberg et al., 2012)	Intron
bmp2b F	GAC GAC TCT CTG TCG TGG GA		Intron
bmp2b R	TTG AAT GCG TTA CCG GAG GA		Intron
bmp4 F	GCG AAC TCC TTT GAG ACC CG		Intron
bmp4 R	GGT CTT CGA TCA CTT CTT GCT GT		Intron
dkk1 F	GCT TGG CAT GGA AGA GTT CG	(Stulberg et al., 2012)	Exon
dkk1 R	AGT GAC GAG CGC AGC AAA GT	(Stulberg et al., 2012)	Exon
eve1 F	TGC GGA AGT GGA TCC TAA CGA		Intron
eve1 R	ACT CGC TGG ACA GAT TTT GAT TCT		Intron
hoxb1b F	CAG CAA GTA TCA GGT CTC CC		Intron
hoxb1b R	CCA TTG TAA CTA GTC ATA ACT CAC		Intron
id1	GCA CTC CGC TCA CAA CAC TCA		Intron
id1 R	GAG TTG GGT CGT TCA GAC AAA CA		Intron
msxe F	CGT TTT CGG TGG AGG TTC TGC		Intron
msxe R	GCG CAC ACG CAT CTG TTG AT		Intron
sef F	TGA GCT CAC AGC CCT TCT CA	(Stulberg et al., 2012)	Intron
sef R	GCA GAA AAG ATG GCG GAA AG	(Stulberg et al., 2012)	Intron
sprouty4 F	ATG AGG ACG AGG AAG GCT CC	(Stulberg et al., 2012)	Exon
sprouty4 R	GCA TTT CTG CGA AAG CTT GG	(Stulberg et al., 2012)	Exon
tbx6l F	TCC ATC CAG ACT CAC CCG CC	(Stulberg et al., 2012)	Exon
tbx6l R	AGT GAA GAA CCA CCA GGC CGT	(Stulberg et al., 2012)	Exon